ISSN 1674-1056
http://cpb.iphy.ac.cn
http://iopscience.iop.org/cpb
中国物理 B
Chinese Physics
中国物理
Chinese Physics B

Metal halide perovskite photodetectors: Material features and device engineering

Ye Wang(王烨), Meng-Lei Gao(高孟磊), Jin-Liang Wu(吴金良), Xing-Wang Zhang(张兴旺)

Citation: Chin. Phys. B . 2019, 28(1): 018502. **doi:** 10.1088/1674-1056/28/1/018502
Journal homepage: http://cpb.iphy.ac.cn; http://iopscience.iop.org/cpb

What follows is a list of articles you may be interested in

Photon-counting chirped amplitude modulation lidar system using superconducting nanowire single-photon detector at 1550-nm wavelength

Hui Zhou(周慧), Yu-Hao He(何宇昊), Chao-Lin Lü(吕超林), Li-Xing You(尤立星), Zhao-Hui Li(李召辉), Guang Wu(吴光), Wei-Jun Zhang(张伟君), Lu Zhang(张露), Xiao-Yu Liu(刘晓宇), Xiao-Yan Yang(杨晓燕), Zhen Wang(王镇)

Chin. Phys. B . 2018, 27(1): 018501. **doi:** 10.1088/1674-1056/27/1/018501

Fabrication and characterization of novel high-speed InGaAs/InP uni-traveling-carrier photodetector for high responsivity

Chen Qing-Tao, Huang Yong-Qing, Fei Jia-Rui, Duan Xiao-Feng, Liu Kai, Liu Feng, Kang Chao, Wang Jun-Chu, Fang Wen-Jing, Ren Xiao-Min

Chin. Phys. B . 2015, 24(10): 108506. **doi:** 10.1088/1674-1056/24/10/108506

Analysis on high speed response of a uni-traveling-carrier double hetero-junction phototransistor

Jiang Zhi-Yun, Xie Hong-Yun, Zhang Liang-Hao, Zhang Wan-Rong, Hu Rui-Xin, Huo Wen-Juan

Chin. Phys. B . 2015, 24(4): 048504. **doi:** 10.1088/1674-1056/24/4/048504

Enhanced near-infrared responsivity of silicon photodetector by the impurity photovoltaic effect

Yuan Ji-Ren, Huang Hai-Bin, Deng Xin-Hua, Liang Xiao-Jun, Zhou Nai-Gen, Zhou Lang

Chin. Phys. B . 2015, 24(4): 048501. **doi:** 10.1088/1674-1056/24/4/048501

Zero-bias high-responsivity high-bandwidth top-illuminated germanium p–i–n photodetectors

Li Chong, Xue Chun-Lai, Liu Zhi, Cheng Bu-Wen, Li Chuan-Bo, Wang Qi-Ming

Chin. Phys. B . 2014, 23(3): 038506. **doi:** 10.1088/1674-1056/23/3/038506

TOPICAL REVIEW — Photodetector: Materials, physics, and applications

Metal halide perovskite photodetectors: Material features and device engineering*

Ye Wang(王烨)[1,2], Meng-Lei Gao(高孟磊)[1,2], Jin-Liang Wu(吴金良)[1,2], and Xing-Wang Zhang(张兴旺)[1,2,†]

[1] *Key Lab of Semiconductor Materials Science, Institute of Semiconductors, Chinese Academy of Sciences, Beijing* 100083, *China*
[2] *College of Materials Science and Opto-Electronic Technology, University of Chinese Academy of Sciences, Beijing* 100049, *China*

(Received 21 September 2018; revised manuscript received 17 October 2018; published online 27 December 2018)

In recent years, the rapid progress of metal halide perovskite solar cells has been witnessed by the rocketing power conversion efficiency. In addition, perovskites have opened up a great opportunity for high performance photodetectors (PDs), due to their attractive optical and electrical properties. This review summarizes the latest progress of perovskite-based PDs, aiming to give a comprehensive understanding of the material design and device engineering in perovskite PDs. To begin with, the performance parameters and device configurations of perovskite PDs are introduced, which are the basis for the next discussion. Next, various PDs based on perovskites in different morphologies are discussed from two aspects: the preparation method, and device performance. Then, several device engineering strategies to enhance the performance of perovskite-based PDs are highlighted, followed by the introduction of flexible and narrow-band perovskite PDs. Finally, key issues and major challenges of perovskite PDs that need to be addressed in the future are outlined.

Keywords: metal halide perovskite, photodetectors, responsivity, solution process

PACS: 85.60.Dw, 85.60.Gz, 81.05.Hd, 81.15.Lm **DOI:** 10.1088/1674-1056/28/1/018502

1. Introduction

Photodetectors (PDs), which operate by converting incident light into electrical signals, are the mainstay of a variety of industrial and scientific applications, such as imaging systems, optical communications, environmental surveillance, and biological sensing.[1–5] The semiconductor, as an active layer, is the essential part of the PD, and can absorb the incident photons and generate electron and hole pairs. Besides, a built-in or applied electric field is necessary to separate the electron and hole pairs, which are collected by electrons to produce an electric current. Up to now, a variety of semiconductors has been applied for conventional PDs, including Si, Ge, group II–VI (PbS and PbSe), group IIB–VI ($Hg_{1-x}Cd_xTe$), and group III–V (GaN and $In_xGa_{1-x}As_yP_{1-y}$). These PDs have been fully investigated and there has been impressive progress on the improvement of photodetection and device configuration design. However, there are several drawbacks, such as the complex manufacturing, high cost, and mechanical inflexibility, which limit broad applications of conventional PDs.

Low-temperature solution-processed semiconductors, such as organic semiconductors, nanomaterials, and quantum dots, are an emerging class of photoactive materials because they are compatible with the simple, low-cost, large area, and flexible manufacturing process.[5] Among them, metal halide perovskites have attracted wide research interests due to their direct bandgaps, long carrier diffusion lengths, high absorption coefficients, and high defect tolerance.[6–10] These outstanding features make metal halide perovskites widely applied in solar cells.[11–14] As a result, the power conversion efficiency of perovskite solar cells has risen from 3.8% to 23.3% in the past few years.[15,16] Based on these significant improvements, the perovskite film formation, chemical composition, and hole/electron transport materials have been amply developed.[17,18] In addition, metal halide perovskites also have great potential in many other optoelectronics, such as light-emitting diodes (LEDs), lasers, and PDs.[19–25] Particularly, there already have been plenty of research studies about perovskite PDs in material compositions and morphologies, as well as device architectures and engineering. Various strategies have been developed to synthesize perovskites in different morphologies (polycrystalline films, single crystals, and low-dimensional nanostructures) for PDs. Meanwhile, device-engineering strategies are applied to improve the performance of the perovskite PDs. Therefore, it is necessary to give a comprehensive review of the perovskite PDs in material compositions and device engineering.

In this review, we first introduce the performance parameters that influence the performance of perovskite PDs, the configurations of which can be divided into three types: photodiodes, photoconductors, and phototransistors. Next,

*Project supported by the National Key Research and Development Program of China (Grant No. 2017YFB0405602), the National Natural Science Foundation of China (Grant Nos. 61674137, U1738114, and 61874106), and the Strategic Priority Research Program on Space Science, the Chinese Academy of Sciences (Grant No. XDA15051200).

†Corresponding author. E-mail: xwzhang@semi.ac.cn

© 2019 Chinese Physical Society and IOP Publishing Ltd

we mainly discuss PDs based on perovskites in different morphologies, including polycrystalline films, single crystals, nanowires/nanorods, quantum dots/nanocrystals, and two-dimensional (2D)/quasi-2D perovskites. Then, several strategies to fabricate high-performance or special-purpose perovskite PDs are illustrated and analyzed. Finally, we provide a brief conclusion and outlook about both the achievement and challenges of perovskite PDs.

2. PD basics

2.1. PD performance parameters

There are several parameters used to evaluate the performance of perovskite PDs, including responsivity R, detectivity D^*, linear dynamic range (LDR), and response time (rise/decay time). A brief overview of these parameters is presented as follows.

2.1.1. Responsivity (R)

The responsivity is defined as the ratio of photocurrent to incident-light intensity, which measures the electrical output per optical input. It is given by

$$R = \frac{J_{\rm ph}}{L_{\rm light}}, \tag{1}$$

where $J_{\rm ph}$ is the photocurrent, and $L_{\rm light}$ is the incident light intensity. The responsivity of a PD is usually expressed in units of amperes per watt of incident radiant power. As defined above, R is proportional to the external quantum efficiency (EQE), which evaluates the conversion rate from photons to electrons/holes of PDs. In consequence, responsivity can also be expressed as

$$R = {\rm EQE}\frac{\lambda e}{hc}, \tag{2}$$

where h is the Planck constant, c refers to the speed of light in a vacuum, λ is the light wavelength, and e refers to the absolute value of electron charge.

Another parameter closely related to responsivity is photoconductive gain G, which is defined as the average number of circuit electrons generated per photocarrier pair.[26] The device responsivity can be calculated from photoconductive gain

$$R = \frac{\eta G \lambda e}{hc}, \tag{3}$$

where η $(0 < \eta < 1)$ is the quantum efficiency, which indicates the probability that a single photon incident on the device will generate a photocarrier pair that contributes to the detector current. So far, the gain G can also be calculated by the measured carrier-recombination lifetime and transit time, which is widely used to estimate the optical gain in photoconductors with the photoconductive effect[27]:

$$G = \frac{\tau}{\tau_{\rm T}} = \frac{\tau}{L/\mu E}, \tag{4}$$

where τ is the excess minority carrier lifetime, and $\tau_{\rm T}$ is the carrier transit time. $\tau_{\rm T}$ can be expressed as $L/\mu E$, where L is the channel length, μ is the carrier mobility, and E is the electric field intensity provided by bias voltage.

2.1.2. Detectivity (D^*)

The specific detectivity D^* characterizes the weakest level light that can be detected by PDs, which is determined by the responsivity and noise of PDs. The D^* is given by

$$D^* = \frac{(A\Delta f)^{\frac{1}{2}}}{i_{\rm noise}/R}, \tag{5}$$

where A is the effective area of PDs, Δf is the electrical bandwidth, and $i_{\rm noise}$ is the noise current. When the dark current is dominated by the shot noise, D^* can be expressed as

$$D^* = \frac{R}{(2qJ_{\rm d})^{\frac{1}{2}}}. \tag{6}$$

Another parameter characterizes the noise level of the detector, and the detector's ability to detect weak light signals is known as the noise equivalent power (NEP), which is defined as the signal incident light power on the PD when the signal-to-noise ratio $S/N = 1$ is detected (the signal-to-noise ratio is the ratio of the effective value of the signal to the effective value of the noise). Since the noise level is proportional to the root of the measurement bandwidth Δf, the NEP specifies measurement results at a 1 Hz bandwidth. Consequently, the NEP is equal to the reciprocal of D^*:

$${\rm NEP} = \frac{(A\Delta f)^{\frac{1}{2}}}{D^*} = \frac{i_{\rm noise}}{R}. \tag{7}$$

2.1.3. LDR

One important characteristic for PDs is the capacity to perform an identical responsivity over a wide range of light intensity, which is known as the LDR:

$${\rm LDR} = 20\log\left(J^*_{\rm ph}/J_{\rm d}\right), \tag{8}$$

where $J^*_{\rm ph}$ is the photocurrent measured at a light intensity of 1 mW·cm^{-2}, and $J_{\rm d}$ is the dark current. The LDR is important because the intensity of the light signal cannot be accurately detected and calculated beyond this range.

2.1.4. Response time (rise/decay time)

PDs are not only evaluated by sensitivity, but also by speed. The response time is characterized by rise time $\tau_{\rm r}$ and fall time $\tau_{\rm f}$ of its response to the optical signal. Generally, the rise time and fall time are the times taken for the photocurrent to rise to 63.2% and drop to 36.8% of the steady-state values, respectively.[25,28] However, when PDs are modulated in a pulsed case, the rise time is defined as the time to transit between 10% to 90% of the peak output value, and vice versa for the fall time.[29–32]

2.2. PD configurations

Generally, there are three main types of configurations for perovskite PDs: photodiodes, photoconductors, and phototransistors.[25,33–37] According to the spatial layout of the photoactive medium and electrodes, perovskite PDs can be divided into two major categories: the lateral type, and the vertical type (Fig. 1(a)).

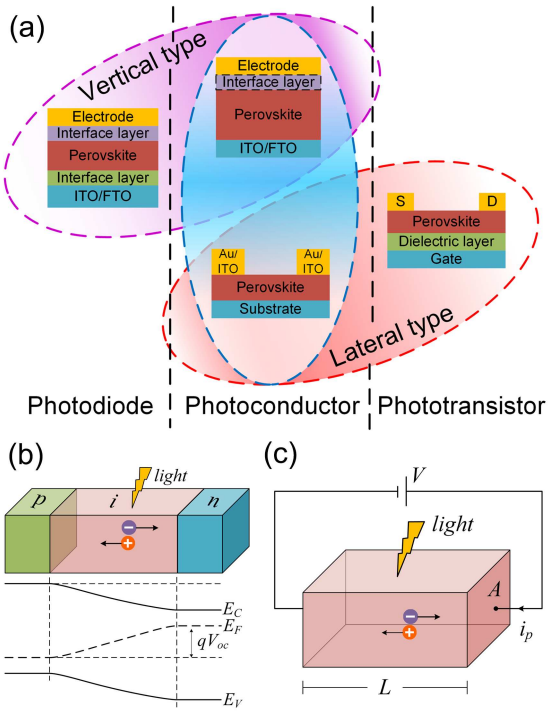


Fig. 1. (a) Categories of perovskite PD configurations. (b) Schematic diagram of photoconductor. (c) Schematic diagram of p–i–n photoconductor.

A photodiode is a p–n junction that has a depleted semiconductor region with a high electric field that serves to separate photogenerated electron–hole pairs. Photodiodes derived from a p–n photodiode include, but are not limited to, the following: p–i–n photodiodes (Fig. 1(b)), heterostructure photodiodes, and Schottky barrier photodiodes.[26] As for perovskite photodiodes, most of them have a p–i–n structure and are very similar in configuration to perovskite solar cells. When the photodiode is under light, photocarriers are separated by the built-in electric field, and the V_{oc} is open-circuit voltage. The difference is that the perovskite photodiode works under a reverse applied field in order to provide a low dark current and a fast response time. Due to the built-in fields at the interface, this type of detector can work at a very low driving voltage or even at 0 V bias.[28,31,38–42] There are hole/electron transporting layers applied to enhance the performance of both devices. Besides, an extra blocking layer to improve the performance ulteriorly has also been introduced.[33,34,38] As shown in Table 1, the perovskite photodiode usually exhibits a low dark current, but it also has a lower photocurrent. As a result, this type of device usually exhibits a high detectivity D^* and a large LDR. In contrast with the photoconductor, the responsivity R_λ and EQE of the photodiode are lower because of the low gain of the photodiode.

A photoconductor is based on the photoconductive effect, in which an electric field applied to the material by an external voltage source causes the electrons and holes to be transported.[26] In comparison to the photodiode, the perovskite photoconductor has a simple configuration and an easy process (Fig. 1(c)); thus, the latter is more convenient to integrate.[43,44] Besides, this type of detector has a larger dark current than photodiodes, which leads to a small detectivity and a narrower LDR (Table 1). The photocurrent amplification in the photoconductor due to the recycling of photoexcited electrons (holes) makes it possible to acquire a high responsivity R_λ and EQE. However, the large gain and EQE of the photoconductor come at the cost of response time because both the gain time and response time are determined by the life time of trapped carriers.[27] Hence, a trade-off between the gain and response times is required in order to achieve optimal device performance. As mentioned above, the perovskite photodiode configurations are vertical and usually include conventional and inverted types (Figs. 2(a) and 2(b)), while perovskite photoconductors can be both lateral and vertical devices (Figs. 2(c) and 2(d)). Lateral structure devices usually employ a perovskite film, and the electrode spacing (> 5 μm) is larger than that of photodiodes (< 1 μm). Due to the simple configuration, lateral structure devices more easily achieve flexibility. For the vertical structure photoconductor, due to the smaller electrode spacing, a high gain can be achieved with a low driving voltage. The active layers of most vertical structure perovskite PDs are made by perovskite single crystals, that is, the dark current is lower due to less defects, and the detectivity is subsequently higher. However, the single-crystal perovskite layer is typically very thick in order to acquire a high responsivity R_λ, which makes the process more difficult than in other types.[36]

As mentioned above, the lateral structure photoconductor is relatively facile to fabricate. However, it usually has a large dark current and a relatively slow response, and thus the phototransistor is designed with a gate electrode to modulate the charge transport. Phototransistors usually have a three-terminal configuration, which is similar to field-effect transistors. The gate electrode is isolated from the perovskite layer by a thin dielectric film, and thus the charge transport can be modulated by applying a gate voltage (Fig. 2(e)). Compared with the lateral structure photoconductor, the gain of the phototransistor is larger due to the modulation by the gate bias; hence, the responsivity and EQE are further improved. Wu and co-workers reported a pure perovskite phototransistor based on solution-processed perovskite films, and provided direct evidence for their superior carrier transport property with ambipolar characteristics.[25] As a result, the phototransistor acquired a large responsivity and an ultrafast response speed, which demonstrated that the phototransistor

configuration is advantageous for enhancing the gain and responsivity without sacrificing the response speed. The fly in the ointment is that the driving voltage of the phototransistor is usually larger than that of other configurations. To further improve the performance of transistors, one feasible approach is hybridization with other materials (Fig. 2(f)), such as 2D layered materials,[45] quantum dots,[46] and plasmonic nanoparticles.[37]

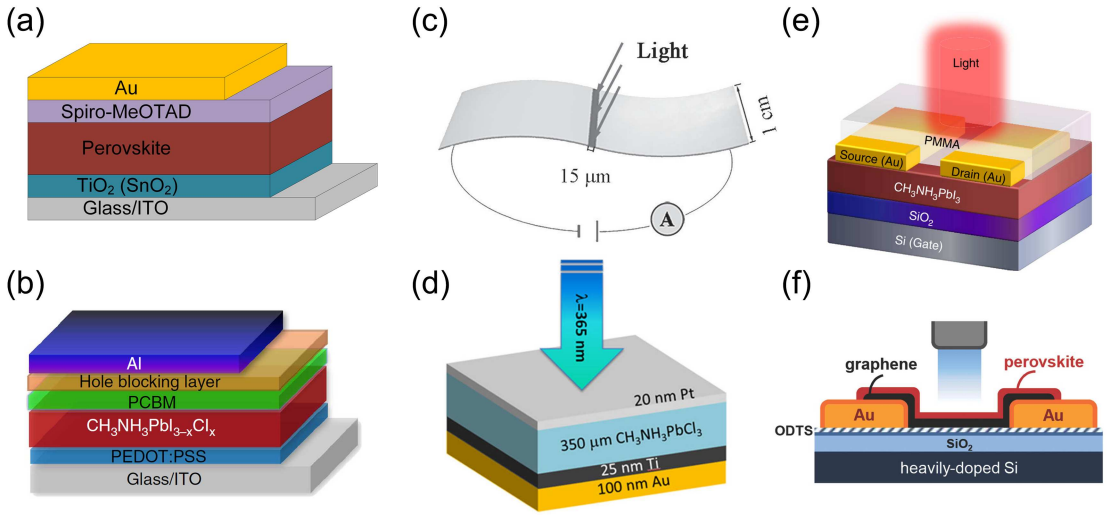


Fig. 2. Different configurations of perovskite PDs, including (a) a conventional photodiode,[34] (b) an inverted photodiode,[38] (c) a lateral photoconductor,[47] (d) a vertical photoconductor,[48] (e) a phototransistor,[25] and (f) a phototransistor with a hybrid functional layer.[45]

Table 1. The advantages and disadvantages of different device configurations.

Performance parameters	Photodiode	Photoconductor (vertical)	Photoconductor (lateral)	Phototransistor
J_d	⋆	⋆⋆⋆⋆	⋆⋆⋆	⋆⋆⋆
On/off ratio	⋆⋆⋆	⋆⋆⋆	⋆⋆⋆⋆⋆	⋆⋆⋆⋆⋆
R_λ	⋆	⋆⋆⋆⋆⋆	⋆⋆⋆⋆	⋆⋆⋆⋆⋆
EQE	⋆	⋆⋆⋆⋆⋆	⋆⋆⋆⋆	⋆⋆⋆⋆⋆
Gain	⋆	⋆⋆⋆⋆⋆	⋆⋆⋆⋆	⋆⋆⋆⋆⋆
D^*	⋆⋆⋆⋆⋆	⋆⋆⋆	⋆⋆⋆	⋆⋆⋆
LDR	⋆⋆⋆⋆⋆	⋆⋆⋆	⋆⋆⋆	⋆⋆⋆
Response time	⋆	⋆⋆⋆	⋆⋆⋆⋆⋆	⋆⋆⋆
Driving voltage	⋆	⋆⋆	⋆⋆⋆	⋆⋆⋆⋆⋆
Complexity	⋆⋆⋆	⋆⋆⋆⋆⋆	⋆	⋆⋆⋆

"⋆" represents the grade of each metric of different type PDs; the greater number of "⋆", the larger the value of the corresponding metric.

3. Perovskite materials

Generally, halide perovskites have the formula ABX_3, in which A and B are cations, and X represents halogen anion (Cl^-, Br^-, and I^-) (Fig. 3(a)). In consideration of the formability[49–51] and photoelectric conversion properties,[52–54] the cations suitable for metal halide perovskites are limited. Small organic molecules (such as $CH_3NH_3^+$ (MA) and $CH(NH_2)_2^+$ (FA)) and inorganic cations (such as Cs^+ and Ru^+) are employed as monovalent A cations. Bivalent transition metal ions (such as Pb^{2+}, Sn^{2+}, Ge^{2+}, and Mn^{2+}) are employed as B cations.

The thermal and structural instability of organic cation lead perovskite is an urgent problem that needs to be solved. Three-dimensional (3D) MA-based perovskites suffer from intrinsic instability due to the relatively volatile MA cations that are released from the film during heating, and this process is accelerated in the presence of moisture. In addition, $MAPbI_3$ was found to be prone to degradation following exposure to moisture, heat, oxygen, and light.[55–58] It was previously reported that FA-based perovskites exhibited much greater thermal stability than MA-based perovskites.[59] Nevertheless, the black perovskite phase of pure $FAPbI_3$ is thermodynamically stable only above 160 °C.[60] Although all-inorganic perovskite ($CsPbI_3$) has better thermal stability, the most stable phase at room temperature is not a black phase with high photoelectric conversion efficiency. Notably, recent studies have revealed that mixed perovskites showed improved stability and device performance. The MA/FA mixture demonstrates that a small amount of MA induces a preferable crystallization of FA perovskite into its photoactive black phase, resulting in a more thermally and structurally stable composition than pure MA or FA compounds.[60,61] Furthermore, by substituting FA with Cs cations, $FAPbI_3$ can be stabilized in the desired black α-phase to form a thermally and structurally stable perovskite.[62,63] Besides, the band gap and the optical absorption band border

can be modulated by the substitution of A cations since the band gap changes from 1.48 eV for $FAPbI_3$ to 1.73 eV for $CsPbI_3$.[64] Although the band gap can also be modulated by the ratio of halogens, the range of the adjustment is limited considering the structural stability of perovskite. By substituting FA with Cs cations, the region of structural instability in the Br–I phase space could be pushed to higher energies, and thus potentially achieve a structurally stable mixed-halide perovskite with a band gap of 1.75 eV.[59] For B cations, the bivalent lead ion is usually the best choice to attain high photoelectric conversion efficiency despite the lead being toxic. Sn, Ge, Bi, Cu, and many other elements have been used for replacing Pb in order to avoid the toxicity to the human body and environment.[65–70]

Different from the 3D perovskites mentioned above, layered perovskites have a general formula of $(RNH_3)_2[ABX_3]_nBX_4$, where R denotes a long chain alkyl or aromatic group (such as aliphatic or aromatic alkyl ammonium), and n is relevant to the number of repeated structural units that contain the A cation[71] (Fig. 3(b)). The perovskite structure changes when n changes from 0 to ∞: $n = 0$, a pure 2D structure with formula of $(RNH_3)_2BX_4$; $n =$ defined integer, a quasi-2D structure; and $n = \infty$, a 3D ABX_3 structure. Up to now, 2D and quasi-2D perovskite have attracted much attention due to their robustness to moisture and high luminescence efficiency.[72–74]

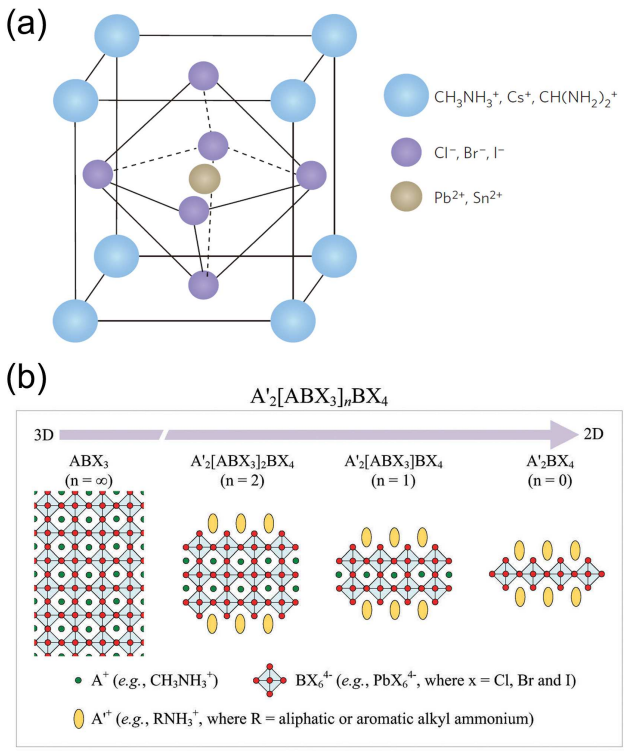


Fig. 3. (a) The structure of perovskites with formula ABX_3, in which A represents cations (MA, FA, and Cs^+), B represents metal cations (Pb^{2+} and Sn^{2+}), and X represents halogen anions (Cl^-, Br^-, and I^-).[75] (b) Schematic structures of 2D $(RNH_3)_2[ABX_3]_nBX_4$ perovskites ($n = 0$, 1, and 2) and 3D ABX_3 perovskite ($n = \infty$), in which A' denotes the RNH_3^+ cations.[71]

As mentioned in Section 1, outstanding physical and chemical properties make perovskite materials the ideal building blocks for constructing different types of optoelectronic devices. Several morphologies of materials are available for different devices. Polycrystalline film is usually the wise choice for a high-efficiency perovskite solar cell, due to the large optical absorption coefficient over a broad wavelength range, ultrafast charge generation, high and microsecond-long balanced mobility, and slow recombination of perovskite materials. For LEDs, nanocrystal, quantum dots, or even 2D perovskite gain much higher luminous efficiency. However, single crystals and nanowires are more suitable for lasers because they require a higher crystal quality. Similarly, perovskites applied in PDs have various morphologies. The representative examples of PDs processed by different types of perovskite materials are presented in Table 2.

3.1. Polycrystalline films

Polycrystalline film is one of the most common types of perovskite materials. There are many universal strategies to form polycrystalline perovskite films, such as thermal annealing, solvent annealing, atmospheric control, solvent engineering, chemical vapor deposition, vacuum flash-assisted solution processing, and the use of additives.[76–84] These strategies have been applied successfully in fabricating not only high-efficiency perovskite solar cells, but also perovskite film PDs. The preparation processes of perovskite polycrystalline films are simple and compatible with different configurations of perovskite PDs, including photoconductors, photodiodes, and phototransistors. Xie and co-workers proposed the first organic–inorganic hybrid perovskite photoconductor, the configuration of which is shown in Fig. 2(c).[47] The active layer was processed by spin-coating the precursor solution on a flexible polyethylene terephthalate (PET) substrate patterned with indium tin oxide (ITO) electrodes. To improve the quality of perovskite films on flexible substrates, Pan and co-workers developed a novel vapor–solution method to achieve uniform and pinhole-free organic–inorganic halide perovskite films on flexible ITO/PET substrates.[84] The preparation process is presented in Fig. 4(a). The PbI_2 layer was first deposited on the patterned ITO/PET substrate, followed by the spin-coating of the MAI layer; then, the substrate with films was annealed at 100 °C for 10 min. The device is shown in Fig. 4(b). These flexible PDs showed an excellent photoresponse with an R value of 81 $A{\cdot}W^{-1}$ at a low working voltage of 1 V (Fig. 4(c)), and exhibited remarkable flexural stability and durability under various bending situations with their optoelectronic performance well retained (Fig. 4(d)). Besides flexible devices, the polycrystalline perovskite films were also deposited on other substrates, such as Si/SiO_2 and ITO/glass to prepare simple but high-photoresponse photoconductors.[19,39,85–87]

Table 2. Materials and key parameters of perovskite PDs.

Device structure/material	Morphology	Sensing light wavelength	Responsivity @ V_{bias} (light source, intensity)	Detectivity D^* @ V_{bias} (light source, intensity)	LDR	Response speed (rise time/fall time)	Ref.
Photoconductor/$MAPbI_3$	polycrystalline films	310–780 nm	3.49 $A{\cdot}W^{-1}$ @ 3 V (365 nm, 0.01 $mW{\cdot}cm^{-2}$)	—	—	< 0.2 s	[47]
Photodiode/$MAPbI_{3-x}Cl_x$	polycrystalline films	300–800 nm	—	8×10^{13} Jones @ −0.1 V (550 nm, 1 $mW{\cdot}cm^{-2}$)	> 100 dB	180 ns/160 ns	[38]
Phototransistor/$MAPbI_3$	polycrystalline films	400–800 nm	320 $A{\cdot}W^{-1}$ @ $V_{DS}=-30$ V, $V_{GS}=-40$ V (white light, 10 $mW{\cdot}cm^{-2}$)	—	—	6.5 μs/5.0 μs	[25]
Photoconductor/$MAPbI_3$	polycrystalline films	300–800 nm	242 $A{\cdot}W^{-1}$ @ −1 V (740 nm)	—	85 dB	10 μs/5.7 μs	[31]
Photoconductor/$MAPbI_{3-x}Cl_x$	polycrystalline films	254 nm	14.5 $A{\cdot}W^{-1}$ @ 2 V (white light, 66 $nW{\cdot}cm^{-2}$)	—	—	0.2 μs/0.7 μs	[85]
Photodiode/$MAPbI_3$	polycrystalline films	300–800 nm	—	~ 3×10^{12} Jones @ 0 V (700 nm)	~ 170 dB	1.7 μs/1.0 μs	[24]
Photodiode/$MAPbCl_3$	single crystals	365 nm	~ 0.05 $A{\cdot}W^{-1}$ @ −15 V (365 nm, 1 $W{\cdot}cm^{-2}$)	1.2×10^{10} Jones	—	24 ms/62 ms	[48]
Photoconductor/$MAPbBr_3$	single crystals	380–600 nm	> 4000 $A{\cdot}W^{-1}$ @ 5 V (525 nm)	> 3×10^{13} Jones	—	~ 25 μs/25 μs	[30]
Photoconductor/$MAPbI_3$	single crystals	275–790 nm	953 $A{\cdot}W^{-1}$ @ 1 V (532 nm, 2.12 $nW{\cdot}cm^{-2}$)	—	76 dB	74 μs/58 μs	[98]
Photodiode/$FAPbI_3$	single crystals	380 nm	0.68 $A{\cdot}W^{-1}$ @ −0.1 V (380 nm, 0.5 $mW{\cdot}cm^{-2}$)	—	—	12.4 ms/17.2 ms	[94]
Photodiode/$CsPbBr_3$	single crystals	410–570 nm	6 $A{\cdot}W^{-1}$ @ −10 V (550 nm)	—	—	—	[95]
Photoconductor/$MAPb(Br_xI_{1-x})_3$	single crystals	405–710 nm	2.36 $A{\cdot}W^{-1}$ @ 2 V (460 nm)	1.15×10^{12} Jones	—	3.4 ms/3.6 ms	[108]
Photodiode/$MAPbBr_3$	single crystals	~ 555–585 nm	—	2×10^{10} Jones @ 4 V (570 nm)	—	~ 1.6 ms	[36]
Photoconductor/$MAPbI_3$	nanowires	400–750 nm	4.95 $A{\cdot}W^{-1}$ @ 1 V (530 nm, 2 $nW{\cdot}cm^{-2}$)	2×10^{13} Jones	—	< 0.1 ms	[120]
Photoconductor/$MAPbI_3$	nanowires	633 nm	5 $mA{\cdot}W^{-1}$ @ 1 V (633 nm, 0.25 $mW{\cdot}cm^{-2}$)	—	—	0.35 ms/0.25 ms	[114]
Photoconductor/$MAPbI_3$	nanowires	532 nm simulated 1 sun	—	—	—	0.12 s/0.21 s	[221]
Photoconductor/$Cs_x(MA)_{1-x}PbI_3$	nanowires	530 nm	23 $A{\cdot}W^{-1}$ @ 5 V (530 nm, 4.5 $mW{\cdot}cm^{-2}$)	2.5×10^{11} Jones	—	—	[113]
Photoconductor/$MAPbI_3$	nanowires	370–780 nm	12500 $A{\cdot}W^{-1}$ @ 5 V (550 nm, 42 $mW{\cdot}cm^{-2}$)	1.73×10^{11} Jones	> 114 dB	0.34 μs/0.42 μs	[123]
Photoconductor/$CsPb(Br/I)_3$	nanowires	532 nm	—	—	—	0.68 s/0.66 s	[112]
Photoconductor/$CsPbI_3$	nanocrystals	470–750 nm	—	—	150 dB	24 ms/29 ms	[140]
Photoconductor/$CsPbI_3$	nanocrystals	470–750 nm	—	—	150 dB	24 ms/29 ms	[140]
Photoconductor/$CsPbBr_3$ + Au nanoparticles	nanocrystals	300–550 nm	~ 0.01 $A{\cdot}W^{-1}$ @ 2 V (520 nm)	4.56×10^{8} Jones	—	0.2 ms/1.2 ms	[137]
Photoconductor/$MAPbI_{3-x}Cl_x$	nanocrystals	300–800 nm	5.6×10^{8} $A{\cdot}W^{-1}$	2.8×10^{16} Jones	92 dB	20 μs/0.445 ms	[222]
Phototransistor/$CsPbBr_{3-x}I_x$–graphene	nanocrystals	400–700 nm	8.2×10^{8} $A{\cdot}W^{-1}$ @ (405 nm, 0.07 $mW{\cdot}cm^{-2}$)	~ 10^{16} Jones @ (405 nm, 0.07 $mW{\cdot}cm^{-2}$)	—	0.81 s/3.65 s	[138]
Photoconductor/$MAPbI_3$	2D/quasi-2D	405 nm	22 $A{\cdot}W^{-1}$ @ 1 V (405 nm)	—	—	20 ms/40 ms	[145]
		532 nm	12 $A{\cdot}W^{-1}$ @ 1 V (532 nm),				
Photoconductor/$(C_4H_9NH_3)_2PbBr_4$–graphene	2D/quasi-2D	470 nm	~ 2100 $A{\cdot}W^{-1}$ @ 0.5 V (470 nm, 1 $mW{\cdot}cm^{-2}$)	—	—	—	[166]
Photoconductor/$CsPbBr_3$	2D/quasi-2D	300–550 nm	0.64 $A{\cdot}W^{-1}$ @ 10 V (517 nm)	—	—	19 μs/25 μs	[143]
Photoconductor/$CsPbBr_3$	2D/quasi-2D	450 nm	—	—	—	17.8 ms/14.7 ms	[144]
Photoconductor/$MAPbI_3$	2D/quasi-2D	simulated 1 sun	~ 0.2 $A{\cdot}W^{-1}$ @ 2 V (white light, 13 $mW{\cdot}cm^{-2}$)	—	—	—	[141]

As for photodiodes, Yang and co-workers presented a solution-processed high-performance PD based on organic–inorganic hybrid $CH_3NH_3PbI_{3-x}Cl_x$ film using an "inverted" device configuration,[38] the energy diagram of which is shown in Fig. 4(e); the photogenerated carriers are separated by the built-in electric field. The ITO side collects electrons, and the Al side collects holes. By adding a hole-blocking layer that used conjugated polymers (2,9-dimethyl-4,7-diphenyl-1,10-phenanthroline (BCP) or poly[(9,9-bis(3'-(*N*,*N*-dimethylamino)propyl)-2,7-fluorene)-alt-2,7-(9,9-dioctylfluorene)] (PFN)), the dark current of the device was greatly reduced (Fig. 4(f)). In addition, the photocurrent remained relatively unchanged at a low voltage range. Thus, the detectivity of the photodiode approached 10^{14} Jones (1 Jones = 1 cm·Hz$^{1/2}$·W^{-1}) at −100 mV, which was one order of magnitude higher than that of the Si PD in the same spectral region. Compared with the photoconductor, the photodiode based on polycrystalline perovskite films showed a faster transient response. Devices with an active area of 0.01 cm^2 showed a rise time of 180 ns and a decay time of 160 ns (Fig. 4(g)). Due to the complex configuration of photodiodes, the performance of devices depends not only on the perovskite layer, but also on the electron/hole transport layer as well as the overall energy level matching of the device. Consequently, improving the device performance by increasing the quality of the perovskite layer is limited.[88,89] There have been several studies about perovskite photodiodes with the similar "inverted" device configuration. To improve the detectivity of devices, inter-layers were added to reduce the dark current.[24,42,90]

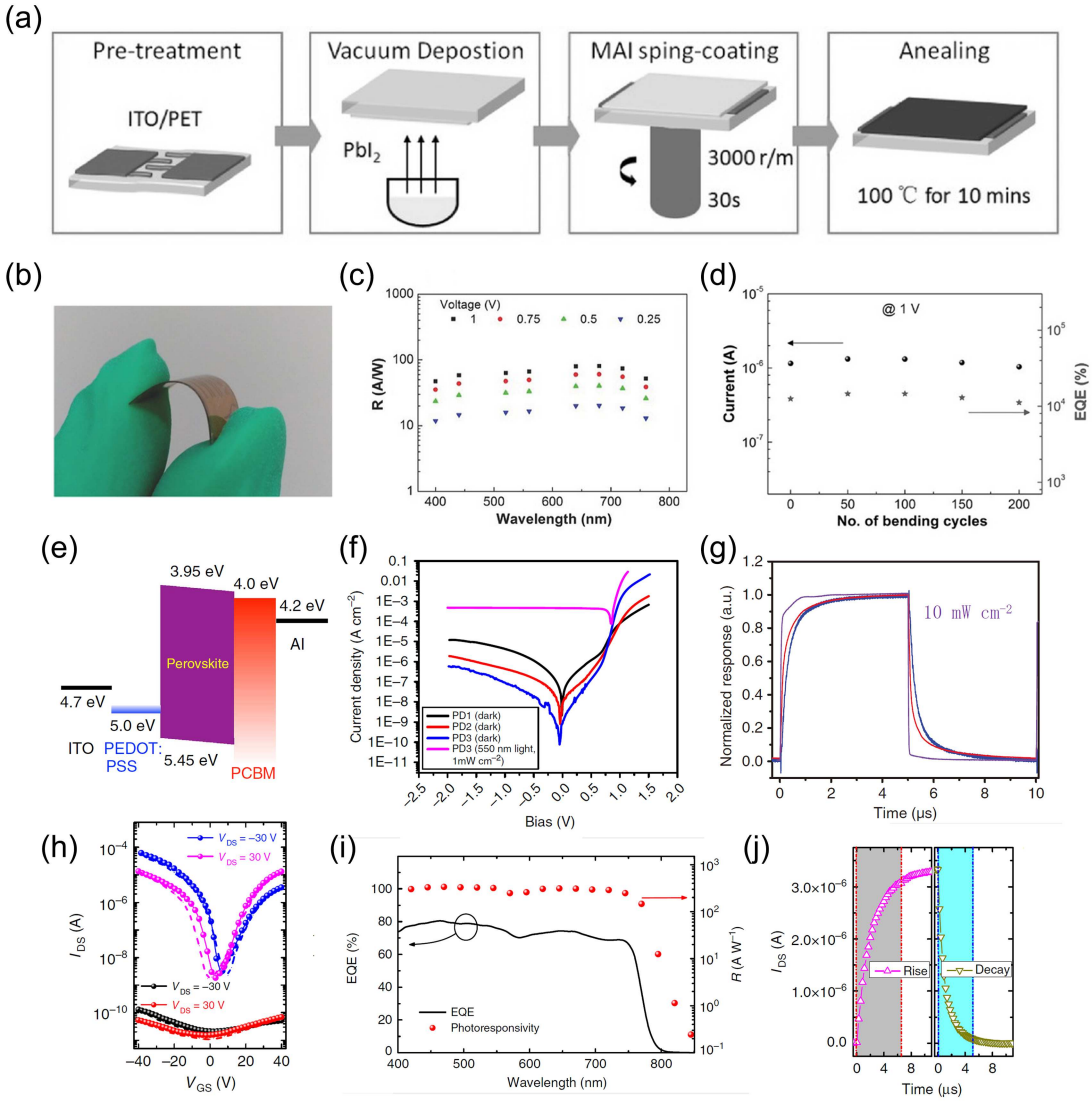


Fig. 4. (a) Fabrication procedure for perovskite thin film using the vapor–solution fabrication method on a patterned ITO/PET substrate. (b) Photograph of a flexible perovskite PD in the bending situation (with interdigital electrodes on the PET substrate). (c) Wavelength-dependent EQE of the flexible PD at different voltages. (d) Photocurrent and EQE of the flexible PD as a function of repetitive bending cycles at 1 V.[84] (e) Energy diagram of the perovskite PD under a slight reverse bias. (f) Current density–voltage curves of PDs with and without the hole-blocking layer. PD1: without hole-blocking layers; PD2 and PD3: with BCP and PFN as the hole-blocking layers, respectively. (g) Transient photocurrent response at a pulse frequency of 100 kHz with a device area of 0.1 cm^2 (blue line) and 0.01 cm^2 (red line). Transient photocurrent response of a silicon diode is shown for comparison.[38] (h) Transfer characteristics of a perovskite-based phototransistor in the dark (black and red symbols) and under light illumination (blue and magenta symbols). (i) EQE and *R* of the hybrid perovskite PD at different wavelengths and a V_{DS} value of −30 V. (j) Temporal photocurrent responses highlighting a rise time of 6.5 μs and a decay time of 5.0 μs.[25]

Although the configuration of the phototransistor is different from that of the photoconductor, the polycrystalline perovskites applied are similar. Wu and co-workers fabricated a phototransistor based on polycrystalline perovskite (Fig. 2(f)), and provided direct evidence for their superior carrier transport property with ambipolar characteristics.[25] The thickness of the perovskite layer is a crucial factor determining the performance of the phototransistor, since one should make a balance between enough light absorption and an effective gate tuning effect. Thus, the optimum perovskite thickness was about 100 nm, and the corresponding phototransistor displayed typical ambipolar I–V curves at drain voltages of −30 V and 30 V (Fig. 4(h)). As we mentioned before, the photoresponse (320 $A\cdot W^{-1}$) and transient response speed (< 10 μs) stayed at a relatively high level (Figs. 4(i) and 4(j)). Different from the general polycrystalline perovskite films, Bakr and co-workers fabricated an orientationally pure crystalline ($MAPbI_3$) hybrid perovskite film by a thermal-gradient-assisted directional crystallization method that relied on the sharp liquid-to-solid transition of $MAPbI_3$ from an ionic liquid solution.[91] Phototransistors based on these perovskite films with low trap-state density and controlled crystal orientation showed a conspicuous photoresponse. Moreover, the demonstration of this unique polycrystalline-based perovskite phototransistor provided an essential guideline for material optimization through crystallization processing and for future developments of novel optoelectronic devices.

3.2. Single crystals

Compared with polycrystalline perovskites, single-crystal perovskites possess many unique properties: high purity, few grain boundaries, and enhanced thermal and moisture stabilities. There are several reported methods for synthesizing perovskite single crystals: inverse temperature crystallization (ITC),[48,92–95] antisolvent vapor-assisted crystallization,[96] top-seed solution growth,[97] bottom-seeded solution growth,[98] and solvent acidolysis crystallization.[99] Among of them, ITC is the simplest and most commonly used approach. It is suitable to use the ITC method when the perovskite exhibits inverse temperature solubility behavior in certain solvents. $MAPbX_3$ perovskites exhibit fascinating inverse solubility trends in solvents like γ-butyrolactone (GBL), N,N-dimethylformamide (DMF), dimethylsulphoxide (DMSO), or their mixtures.[92] As shown in Fig. 5(a), the precursor solutions were heated from room temperature and kept at an elevated temperature to initiate crystallization. For $MAPbBr_3$, by setting the temperature of the heating bath at 80 °C, usually < 5 crystals were formed in the case of a 1 M solution of $PbBr_2$ and MABr in DMF. Unlike $MAPbBr_3$, ITC of $MAPbI_3$ was only possible in GBL solution (no precipitates were observed in DMF or DMSO), with the bath temperature set to 110 °C. It is also worth noting that neither of the precursors PbX_2 and MAX showed any reverse dissolution behavior (i.e. the saturated solution of a single precursor did not show precipitation upon heating), thus suggesting that this phenomenon was related to the perovskite structure. In particular, the growth rate (maximum at 38 $mm^3\cdot h^{-1}$) of the crystal was an order of magnitude greater than the previously reported highest growth rate.[100] Besides, the high-quality single crystalline properties of large grain size, few grain boundaries, high charge carrier mobility, low trap density, long charge carrier diffusion lengths, fast-component excitons lifetimes, and slow-component lifetimes, were confirmed by various characterization techniques such as single-crystal x-ray diffraction analysis, steady-state absorption and photoluminescence, and carrier lifetime measurements. With these outstanding characteristics, perovskite single crystals have been applied in PDs with unique functions, including narrowband PDs,[36,101] integrated PDs,[43,102] visible-blind ultraviolet (UV)-PDs,[48,103] self-powered PDs,[104,105] and high-energy ray photon detection PDs.[106,107] Huang and co-workers fabricated hybrid perovskite single-crystal vertical photoconductors that have a very narrow spectral response.[36] The thickness of the perovskite layer was about 1 mm, much thicker than the polycrystalline perovskite layer applied in PDs (Fig. 5(b)). There was a surface-charge recombination-enabled narrowband photodetection mechanism. The charge carriers are generated mostly in a narrow region near the Au electrode since the light penetration depth is very small (< 300 nm) due to the large absorption coefficient of the hybrid perovskite materials. Thus, the charges generated by the above-bandgap photoexcitation can be quenched easily because of the severe surface-charge recombination. Furthermore, the EQE of PDs was greatly influenced by the bias voltage (Fig. 5(c)) and the thickness of the perovskite layer (Fig. 5(d)). Above all, the device showed an ultra-narrow EQE peak with a full width at half maximum (FWHM) of < 20 nm, a high sensitivity with a detection limit down to 80 $pW\cdot cm^{-2}$, and a high off-resonance rejection ratio of > 200. Thinking outside the simple single crystalline perovskite photoconductors,[98,108] Liu and co-workers designed and constructed a large-area (≈ 1300 mm^2) imaging assembly composed of a 729 pixel sensor array (Fig. 5(e)).[102] The detectivity and EQE of the PD are presented in Fig. 5(f), in which the detectivity is as high as 6×10^{13} Jones, much better than commercial sensors made of silicon and InGaAs. It is contemplated that the combination of commercial chip fabrication that offers much higher resolution and the superior perovskite single crystal with high optoelectronic quality can lead to a wide range of applications such as high-speed and high-detectivity sensors, electronic eyes, etc.

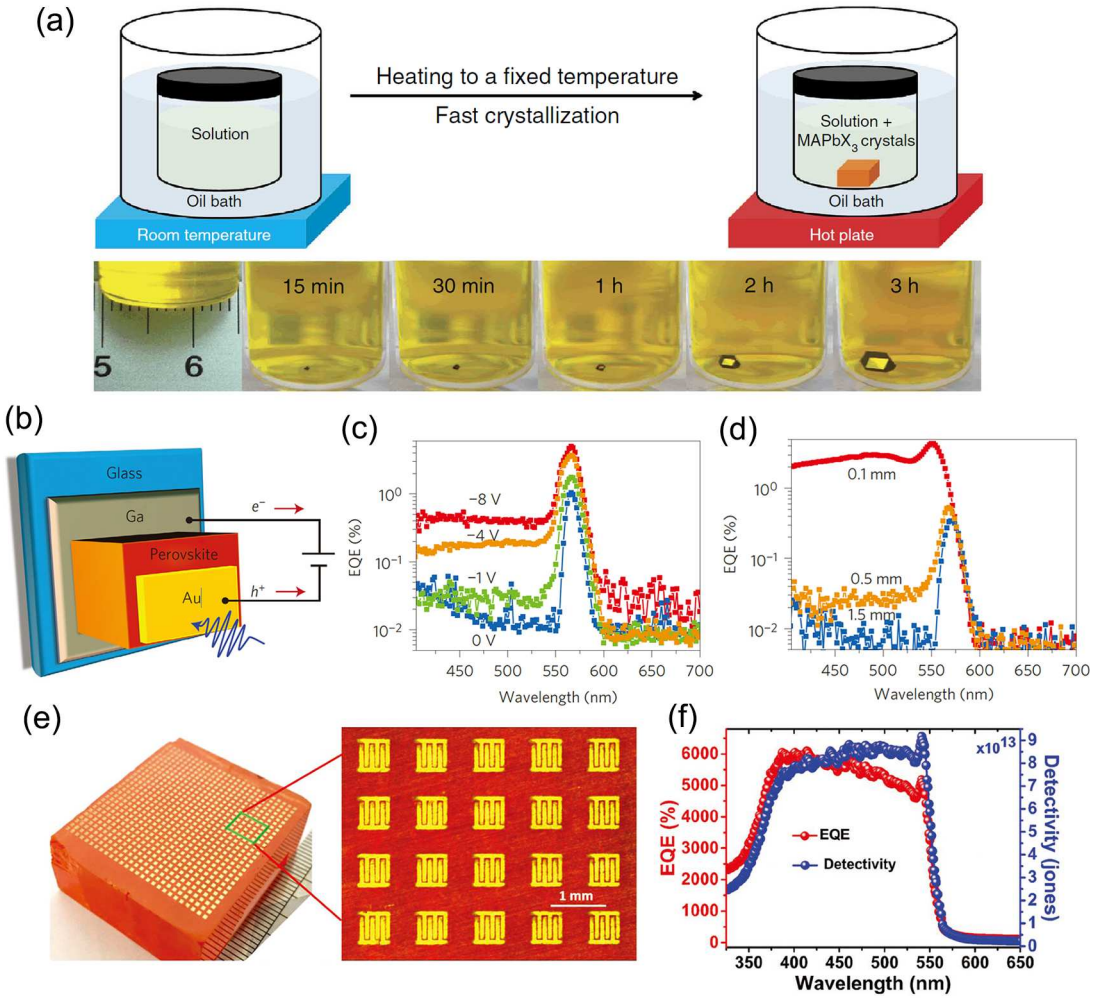


Fig. 5. (a) Schematic of the ITC apparatus and $MAPbI_3$ crystal growth at different time intervals.[92] (b) Device structure of a single-crystal perovskite PD. (c) EQE spectra of a 0.3 mm thick $MAPbBr_3$ single crystal under different reverse biases. (d) EQE spectra of $MAPbBr_3$ single crystals with different thicknesses cleaved from the same large single crystal, measured under a −4 V bias.[36] (e) Photograph of a 27×27 photoconductor array fabricated on a 34×38 mm^2-sized $MAPbBr_3$ single crystal. (f) EQE and detectivity of the $MAPbBr_3$ single crystal photoconductor illuminated by monochromatic light with its wavelength changing from 325 nm to 650 nm at a 4 V bias.[102]

3.3. Nanowires/nanorods

There have been extensive researches about one-dimensional (1D) nanowire materials, such as carbon nanotubes, metal nanowires, metal oxide nanowires, and polymer nanowires, due to their high aspect ratio in conjunction with superior mechanical, electronic, and optical properties.[109,110] Hence, it is desirable to fabricate perovskite nanowires based optoelectronics. Generally, perovskite nanowires are prepared by the solution-phase synthesis method.[111–114] Xue and co-workers demonstrated a simple and effective method of hot-injection for synthesis of $CsPb(Br/I)_3$ nanorods with a uniform rod-shaped structure,[112] the synthesis process of which is shown in Fig. 6(a). Cesium stock solution was obtained by dissolving the $CsCO_3$ powder in oleic acid (OA) and octadecene (ODE) mixture. Meanwhile, the perovskite precursor solution was obtained by mixing $PbBr_2$ and PbI_2 in ODE. After heating at certain conditions, the $CsPb(Br/I)_3$ nanorods were synthesized by injecting cesium stock solution into the precursor solution. The photoresponse of a prototypical PD based on the $CsPb(Br/I)_3$ nanorods was studied by dropping the nanorods dissolved in toluene onto a gold interdigital electrode on a SiO_2 substrate (Fig. 6(b)). The on/off ratio of the nanorod-based PD reached $\sim$ 2000, which makes it have vast application prospects in photoelectric devices. Besides, Horváth and co-workers prepared $MAPbI_3$ nanowires through a simple slip-coating approach,[114] which opens up a new strategy toward low-temperature, solution-processed perovskite films with controlled morphology. Moreover, the $MAPbI_3$ nanowires can be easily combined with monolayer graphene or carbon nanotubes to form heterostructures.[115,116] They also reported a $MAPbI_3$ nanowire PD prepared by the graph epitaxial liquid–solid method, in which the nanowires were crystallized in the arrays of nanofabricated channels owing to the strong guiding effect of the nanogrooves.[117]

Based on the simple solution-phase method, there are several strategies to boost the performance of perovskite

nanowires, including the self-assembly method and template-assisted method. Song and co-workers used the one-step self-assembly method to grow $CH_3NH_3PbI_3$ nanowires,[118] and further applied an evaporation-induced self-assembly (EISA) method to prepare high-ordered perovskite nanowires.[119] In order to obtain a large-area aligned nanowire distribution, the substrates were tilted for a small angle of less than 15° to guide the nanowire alignment (Figs. 6(c) and 6(d)). Perovskite nanowires prepared by EISA have an average diameter of 500 nm and length of 800 μm. The PDs fabricated by the high-ordered perovskite nanowires obtained a responsivity as ~ 1.3 A·W^{-1}, detectivity of 2.5×10^{12} Jones, and response time of ~ 3 ms, which are superior to the recently reported PD performances based on organic–inorganic thin films and inorganic nanowires. Similarly, Tang and co-workers prepared single-crystalline $MAPbI_3$ nanowires using the one-step self-assembly method,[120] and they subsequently introduced OA soaking to passivate surface defects of perovskite nanowires. Thus, the PDs based on perovskite nanowires exhibited much improved stability and outstanding sensitivity (measured detectivity of 2×10^{13} Jones). Yang and co-workers reported highly oriented and ultra-long $MAPbI_3$ nanowire arrays fabricated by large-scale roll-to-roll micro-gravure printing and doctor blading in ambient environments.[121] It provided low-cost, large-scale techniques to fabricate large-area perovskite nanowire arrays, which showed great potential application in flexible electronic and optoelectronic devices.

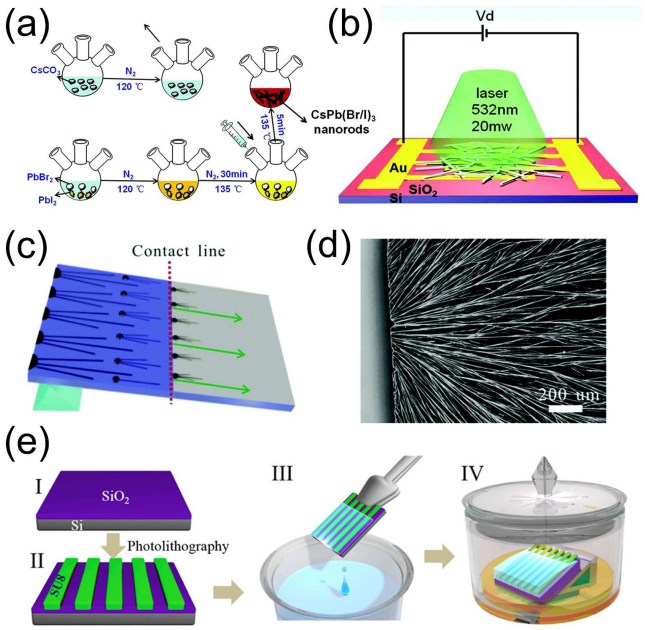


Fig. 6. (a) Schematic diagram of the synthesis process for $CsPb(Br/I)_3$ nanorods. (b) Schematic diagram of the PD based on $CsPb(Br/I)_3$ nanorods.[112] (c) Schematic description of the aligned nanowire growth. (d) Optical images of nanowires grown by a modified EISA method.[119] (e) Schematic illustration of the fluid-guided antisolvent vapor-assisted crystallization (FGAVC) method for the fabrication of the $MAPbI_3$ nanowire array.[123]

Besides the commonly used self-assembly method, the template-assisted method opened up another avenue for high-performance perovskite nanowire PDs. Zhang and co-workers demonstrated a facile method for preparing porous $MAPbBr_3$ nanowires by a self-template-directed reaction of Pb-containing nanowires with HBr and MABr at room temperature in solution.[122] Jie and co-workers reported a facile FGAVC method for large-scale fabrication of high-quality single-crystalline perovskite nanowire arrays.[123] As shown in Fig. 6(e), periodically aligned SU-8 photoresist stripes were fabricated on the SiO_2/Si substrate by photolithography. The SU-8 photoresist template was subsequently dipped into perovskite precursor solutions for a few seconds and placed on a tilted glass ($\sim 5°$) in a weighing bottle together with 3 mL of CH_2Cl_2 solvent. The antisolvent vapor would gradually diffuse into the precursor solution, leading to the crystallization of the $MAPbI_3$ nanowires along the sides of SU-8 photoresist strips. The PDs using the perovskite nanowires prepared by the FGAVC method demonstrated a maximum R value of 1.26×10^4 A·W^{-1} and a high gain of 10^4.

3.4. Quantum dots/nanocrystals

When the size of 3D materials is decreased to the nanometric scale, the tiny spherical particles will exhibit completely different optical and electronic properties compared with their bulk counterparts. Their size-dependent optical band gaps, size tunability, large extinction coefficient, high photoluminescence quantum yield (PLQY), and multiple exciton generation characteristics of quantum dots make them especially suitable for use in optoelectronic devices.[124–128] Perovskite quantum dots/nanocrystals also exhibit quantum-size effects similar to conventional quantum dots, and thus they can be applied in optoelectronic devices.

Generally, two methods have been widely used for the preparation of perovskite quantum dots/nanocrystals: (i) the ligand-assisted re-precipitation (LARP) method[129,130] and (ii) the hot-injection method.[99,131,132] Pérez-Prieto and co-workers first demonstrated solution-phase synthesis of perovskite colloidal quantum dots, in which the $MAPbBr_3$ quantum dots with a size of 6 nm were prepared via re-precipitation using medium-length alkyl chain organic ammonium cations as ligands.[133] Dong and co-workers also reported a simple and versatile LARP technique for the fabrication of $MAPbX_3$ QDs with absolute PLQYs of 50%–70%.[130] The process for the LARP technique and reaction system is illustrated in Fig. 7(a). The precursor solution was formed by dissolving $PbBr_2$, MABr, n-octylamine, and OA into DMF. The precursor solution was subsequently dropped into toluene under vigorous stirring, and it aggregated into nanoparticles after the

colloidal solution turned yellow-green. The colloidal solution in toluene was centrifuged to discard large particles, and a high-quality colloidal solution made of small-sized nanoparticle was attained.

According to the results of early research work, perovskite quantum dots/nanocrystals were most applied in LEDs.[130,131,134] However, more and more studies suggested that PDs based on perovskite quantum dots/nanocrystals also have good performance.[135–139] Early in 2013, Wang and co-workers reported a $CsPbBr_3$ quantum dot PD, the performance of which was enhanced by employing a bilayer composite film of mesoporous TiO_2 (mp-TiO_2) $CsPbBr_3$ quantum dots as photosensitizers.[135] As a result, this PD demonstrated a significantly improved on/off ratio by about three orders of magnitude. Song and co-workers synthesized $MAPbBr_3$ plate-type nanocrystals by a novel solution reaction using octylamine as the capping ligand.[136] The synthesis of $MAPbBr_{3-x}Cl_x$ and $MAPbBr_{3-x}I_x$ nanocrystals was achieved by the halide exchange reaction of $MAPbBr_3$ with MACl and MAI in an isopropyl alcohol solution, respectively, and the nanocrystals with different chemical compositions demonstrated full-range band gap tuning over a wide range (1.6–3 eV) (Fig. 7(b)). Moreover, PDs based on these perovskite nanocrystals showed different photoresponses depending on the halides types. For the PDs based on pure $MAPbBr_3$ nanocrystals, the I–V curves are almost linear within the measured range (−2 V to 2 V), with a dark current of ∼ 1 pA and a photocurrent of 0.24 μA under 365 nm and 505 nm laser irradiation, respectively (Fig. 7(c)). For PDs based on mixed perovskite nanocrystals, photocurrents of those with Cl-rich composition ($MAPbBr_{3-x}Cl_x$) decreased with the increase in x, while those with I-rich composition ($MAPbBrI_2$) exhibited the highest photoconversion efficiency (Fig. 7(d)). A strong correlation was observed between the photocurrent and photoluminescence decay time, and was rooted in the nature of the crystalline structure. Thus, the tetragonal phase exhibits higher photoconversion efficiency than that of a cubic phase. Based on the above results, the same group reported a new method, i.e. ultrasonic irradiation of precursor solutions, for synthesizing $APbX_3$ perovskite nanocrystals, where A = MA, Cs, or FA, and X = Cl, Br, or I.[139] Band gap tuning of the nanocrystals over a wide range (1.54–3.18 eV) was achieved by controlling the composition of cations (MA, Cs, and FA) and halide anions (Cl, Br, or I). The corresponding PDs were fabricated by spin-coating the $APbBr_3$ and $APbI_3$ nanocrystals between Au electrodes patterned on SiO_x substrates, and demonstrated a high on/off ratio over 10^5 at 2 V and under 365 nm illumination.

Since the long-term stability became a major concern for perovskite nanocrystalline applications, all-inorganic perovskite nanocrystals gradually showed advantages owing to their superior stability against oxygen and moisture. Lee and co-workers presented PDs based on all-inorganic $CsPbX_3$ nanocrystals that were synthesized by a hot-injection method.[140] Besides, the $CsPbCl_3$ and $CsPbI_3$ were acquired by halide exchange reactions using lithium salts (LiX, X = Cl, Br, and I). PDs made of $CsPbI_3$ nanocrystals exhibited a high on/off photocurrent ratio of 10^5, as well as rise and decay times of 24 ms and 29 ms, respectively. The same group also demonstrated a high-sensitivity hybrid PD based on graphene–$CsPbBr_{3-x}I_x$ perovskite nanocrystals, which exhibits a high photo-responsivity of $\sim 10^8$ A·W^{-1} and detectivity of $\sim 10^{16}$ Jones under 405 nm and 0.07 mW·cm^{-2} illumination.

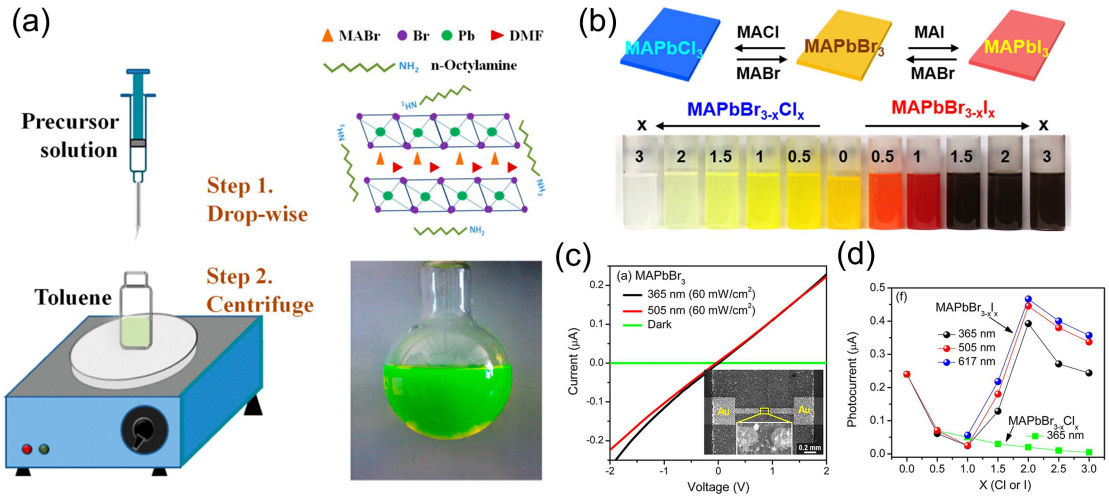


Fig. 7. (a) Schematic illustration of the reaction system and process for the LARP technique. The starting materials in the precursor solution (top right) and the typical optical image of the colloidal $MAPbBr_3$ solution (bottom right) are illustrated.[130] (b) The reversible anion exchange reaction of $MAPbX_3$ nanocrystals. (c) I–V curves of $MAPbBr_3$ film under 365 nm and 505 nm irradiation (60 mW·cm^{-2}) and dark conditions. The inset shows an SEM image of $MAPbBr_3$ film deposited on Au electrodes with a 2 μm gap. (d) Photocurrents of $MAPbBr_{3-x}Cl_x$ and $MAPbBr_{3-x}I_x$ as a function of x at different wavelength irradiations.[136]

3.5. 2D/quasi-2D perovskites

In recent years, 2D materials have been extensively investigated to be applied in PDs due to their excellent optical, electrical, and mechanical properties. Hence, it is desirable to reduce the dimensionality of bulk perovskite to 2D and investigate the optical–electrical characteristic of 2D perovskite-based devices. Currently, 2D perovskite materials can be divided into two types: the non-van der Waals type, and the van der Waals type. The former is derived from a 3D perovskite framework by cutting down the thickness to a single or few unit cells, such as nanoplates,[141] nanosheets,[142–145] and nanoflakes.[146] The latter is built by inserting long-chain organic cations in the "A" position to block the interaction of inorganic $[BX_6]^{4-}$ bilayers, mainly including those quasi-2D perovskites with a formula of $(RNH_3)_2[ABX_3]_nBX_4$ ($n = 0, 1, 2, \ldots$).[147–150]

For non-van der Waals-type 2D perovskites, there are several ways to realize the synthesis process, including the simple solution-phase method, the solution process combined with the vapor-phase conversion method, and the seed-mediated solution growth method. Bao and co-workers reported a combined solution process and vapor-phase conversion method to synthesize 2D hybrid organic–inorganic perovskite (Fig. 8(a)).[145] The PbI_2 aqueous solution was first casted onto a SiO_2 substrate, which was subsequently heated to a fixed temperature facilitating the nucleation of 2D PbI_2 nanosheets. Then, the vaporized MAI was intercalated into the interval sites of PbI_6 octahedron layers to form the 2D $MAPbI_3$ nanosheets. The growth mechanism of the perovskite nanosheets indicated that the out-of-plane growth rate along the *c*-axis is much lower than that of the in-plane one because of the lower surface energy along the in-plane direction. The as-synthesized nanosheets had a relatively smooth surface with a roughness of 0.2–1.0 nm, and the height profiles depicted the single-layer $MAPbI_3$ nanosheets with thicknesses of 1.3 nm (Fig. 8(b)). The schematic diagram of the PDs based

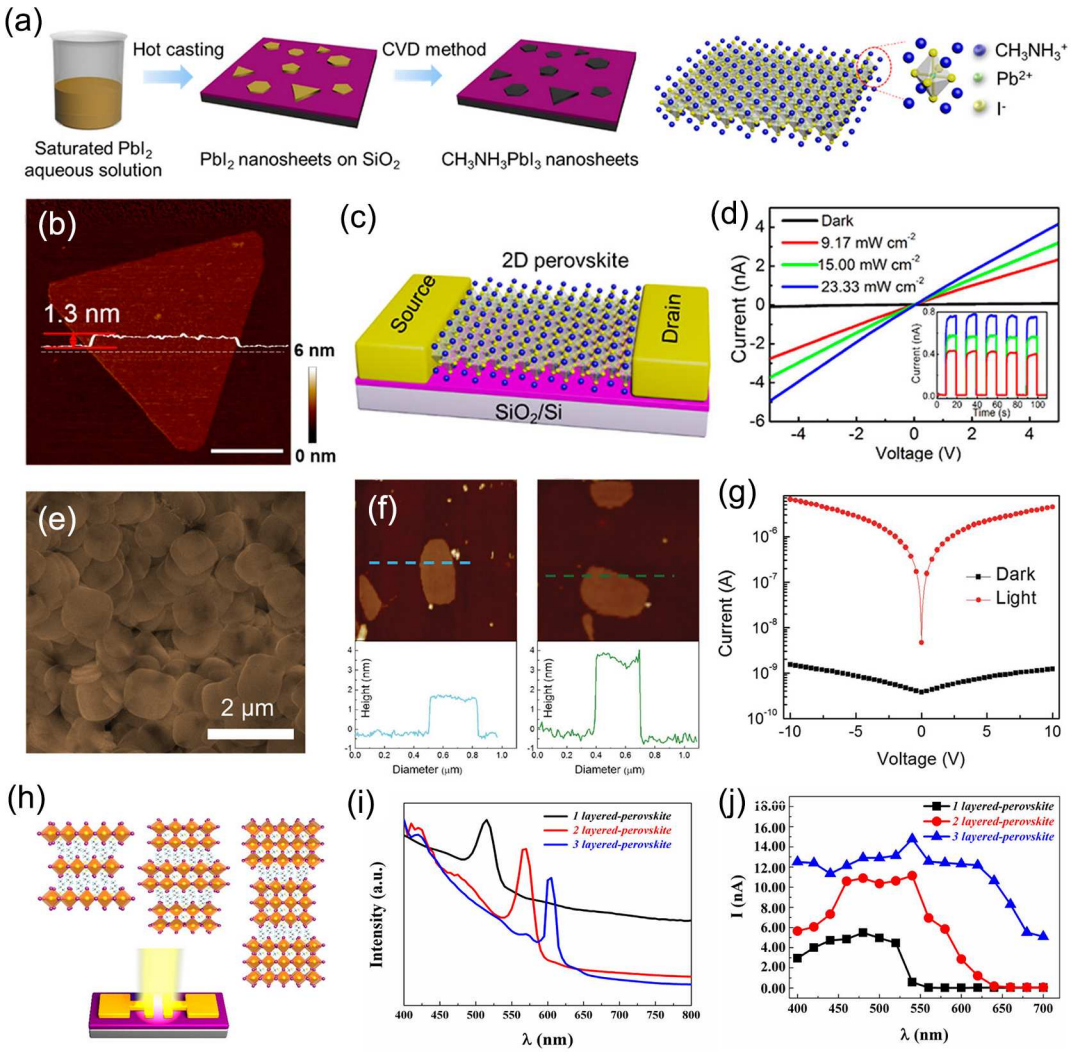


Fig. 8. (a) Schematic illustrations of solution process to fabricate 2D PbI_2 nanosheets, vapor-phase conversion process to transfer PbI_2 to 2D $MAPbI_3$ perovskite nanosheets, and the crystal structure of single unit cell thick 2D $MAPbI_3$ perovskite. (b) Atomic force microscope (AFM) topography images of 2D $MAPbI_3$ nanosheets. (c) Schematic image of a transistor device based on 2D perovskite. (d) *I*–*V* curves of the 2D perovskite-based device under different light intensities.[145] (e) High-magnification SEM images of 2D ultrathin $CsPbBr_3$ nanosheets. (f) AFM image and height profile of monolayer and bilayer $CsPbBr_3$ nanosheets with a thickness of 1.6 nm and 3.3 ± 0.2 nm, respectively. (g) *I*–*V* curves of the PD in the dark and under 442 nm light (0.35 $mW{\cdot}cm^{-2}$).[143] (h) Schematic diagrams of different layer-structured perovskite materials and the perovskite-based PD. (i) Ultraviolet–visible (UV–vis) absorption spectra for layer-structured perovskite materials. (j) Wavelength-dependent photocurrent of the devices with a bias of 30 V.[154]

on these materials is shown in Fig. 8(c). The PDs showed linear I–V curves under different powers of illumination, and the dark current was rather low (10^{-9} A) (Fig. 8(d)). Thus, the responsivity of the PDs was as high as 22 A·W^{-1} at 1 V bias irradiated by a weak laser ($<$ 10 nW), and the response time was 40 ms. Wang and co-workers prepared large arrays of perovskite microplates by a similar method.[151] The arrays of lead iodide microplates were grown from an aqueous solution through a seeded growth process, followed by intercalating MAI to produce perovskite crystals. In particular, the microplates can be selectively grown on pre-patterned electrode arrays to create independently addressable PD arrays and functional field effect transistors.

Song and co-workers reported high-performance flexible visible light PDs based on 2D $CsPbBr_3$ nanosheets.[143] The high-quality and easily dispersed $CsPbBr_3$ nanosheets (Fig. 8(e)) were prepared by using long-chain alkyl amines and OAs as the surfactants that served as growth-directing soft templates, which broke the crystal's inherent cubic symmetry and guided the 2D growth. In addition, the thicknesses were about 1.68 nm and 3.3 nm (Fig. 8(f)) for the as-synthesized monolayer and bilayer nanosheets, respectively, and the edge length was about 1 μm. The flexible PDs based on the $CsPbBr_3$ nanosheet exhibited excellent electron transport properties, a high sensitivity with a light on/off ratio of $> 10^3$ (Fig. 8(g)) under 442 nm light at a power of 0.35 mW·cm^{-2}, as well as high stability and outstanding flexibility ($>$ 10000 cycles). This gives great potential to prepare ultrathin and flexible solution-based optoelectronics based on 2D perovskites.

Van der Waals-type 2D perovskites, namely, the quasi-2D perovskite, can be synthesized by non-colloidal and colloidal methods.[71] Most of the non-colloidal methods, such as the liquid-phase crystallization method[152] and direct solution-phase growth,[153], produce small crystals in solution, which are not suitable for large-area optoelectronics requiring thickness control and complete surface coverage. On the contrary, the colloidal method is easy and has a low cost associated with preparing large-area thin films. Huang and co-workers reported PDs based on 2D layer-structured perovskite with a formula of $(C_4H_9NH_3)_2(CH_3NH_3)_{n-1}Pb_nI_{3n+1}$ (n = 1, 2, and 3).[154] The perovskite film of three different 2D layer-structured perovskite materials with different layer numbers (n = 1, 2, and 3) were fabricated by spin-coating followed by thermal annealing. The structures of the layered perovskite and PDs are illustrated in Fig. 8(h). The optical band gaps of 2D perovskite with different layers were different, which could be clearly observed in the UV–vis absorption spectrum (Fig. 8(i)). Furthermore, the wavelength-dependent output currents of the layer-structured perovskite PDs were closely related to their optical band gaps. The photocurrents remained almost constant with illuminating wavelength larger than their corresponding "threshold" wavelengths, and then increased substantially when the wavelength was below the "threshold" wavelength (Fig. 8(j)). Besides, the more layers of the 2D perovskite, the higher the photocurrent of the PDs.

4. Device engineering

Although there are various perovskite materials for PDs, it is not enough to meet the requirements of high-performance, diverse applications, and high stability, since the different types of perovskites mentioned above have their respective shortcomings. Hence, besides the perovskite materials, device engineering of the PDs is crucial. There are highly developed strategies for perovskite PDs, such as hybridizing with other materials and interface/band gap engineering. In addition, devices with special functions, such as flexible and narrow-band perovskite PDs also enlarge the application field of perovskites.

4.1. Hybrid structure perovskite PDs

It is a common approach to improve the performance of 2D-material PDs using hybrid systems.[155,156] In addition, the hybrid structure of perovskites has been widely applied in solar cells. Therefore, it is rational to employ the hybrid structure to boost the performance of perovskite PDs. There are various materials for hybrid perovskite PDs, such as 2D materials, polymers, metal oxides, and quantum dots.

4.1.1. 2D materials

In recent years, conventional 2D materials, which have excellent optical, electric, thermal, and mechanical properties, have been widely explored as functional layers for PDs.[155] Accordingly, many 2D materials have been studied as functional layers in PDs hybridized with perovskites. These 2D materials include, but are not limited to, graphene and its derivatives,[37,45,138,157,158] transition-metal dichalcogenides (TMDs) (such as MoS_2 and WS_2),[159–161] and h-BN.[162]

Cho and co-workers first fabricated a novel phototransistor consisting of graphene/$MAPbI_3$ hybrid layers.[45] The schematic diagram of the phototransistor is illustrated in Fig. 2(f). The heavily n-doped Si wafer and thermally grown 300 nm thick SiO_2 layer served as the gate electrode and dielectric, respectively, on which the n-octadecyltrimethoxysilane layer was used for reducing surface charge trap sites. As a result, the responsivity and EQE of the PDs were 180 A·W^{-1} and 5×10^4%, respectively. The high performances of the hybrid PD were attributed to the efficient charge transfer from the graphene to the perovskite. On this basis, Sun and co-workers reported a one-

step, solvent-induced, fast crystallization deposition method to produce isolated perovskite islands on a graphene sheet for transistor channel materials. The phototransistor showed an extremely high responsivity of $\approx 6.0 \times 10^5$ A·W^{-1} and a photoconductive gain of $\approx 10^9$ electrons per photon. Besides, graphene derivatives, such as reduced graphene oxide (rGO) and graphene quantum dots (GQD), were also reported to enhance the perovskite PDs.[157,163] Liu and co-workers reported controlled synthesis of a 2D-material/perovskite van der Waals solid, which paved the way for subsequent applications of hybridizing graphene derivatives with perovskite.[164] Shi and co-workers reported a high-performance nitrogen-doped GQD (NGQDs)–perovskite/mildly rGO hybrid phototransistor, in which NGQDs and rGO offered an effective and fast path for electron transfer.[163] The same group also fabricated a high-performance lead-free 2D perovskite flexible PD (with a responsivity of 16 A·W^{-1} and a detectivity of 1.92×10^{11} Jones under 470 nm illumination) employing rGO–P60 as transparent flexible electrodes.[165] In addition, the perovskites in the hybrid structure PDs are not limited to films, but also include nanocrystals,[138] nanowires,[115] and 2D perovskites.[166]

For TMDs, Wu and co-workers fabricated high-performance PDs based on perovskite $MAPbI_3/WS_2$ hybrid layers for the first time.[159] The schematic device structure of the PDs is shown in Fig. 9(a). The WS_2 monolayer was grown on sapphire substrates using chemical vapor deposition methods, and the perovskite layer was deposited by a thermal evaporation method. Due to the superior properties of both perovskite and WS_2, the hybrid structure PDs exhibited high responsivity (≈ 17 A·W^{-1}) and high detectivity (2×10^{12} Jones). The on/off ratio of the hybrid device was enhanced by approximately two orders of magnitude (Fig. 9(b)) compared with the reference perovskite single-layer device. The response speed was also promoted by four orders of magnitude, owing to the high mobility of the WS_2 monolayer and the efficient interfacial charge separation. Above all, 2D materials in the hybrid structure perovskite PDs enhance the charge transfer, thus improving the performance of the PDs.

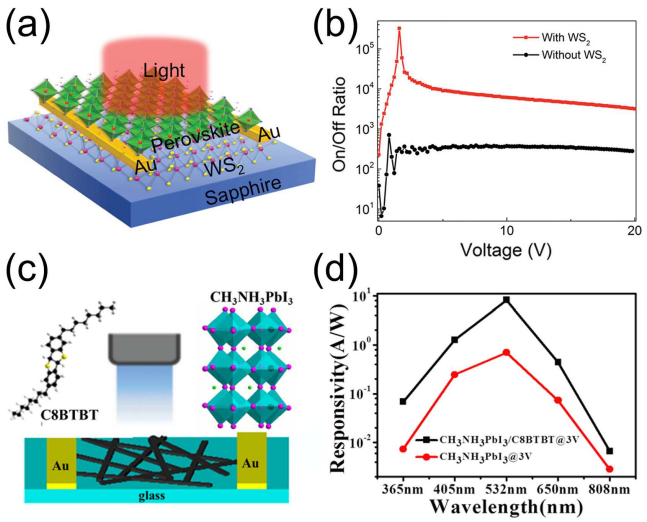


Fig. 9. (a) Schematic device structure of the hybrid WS_2/perovskite photoconductor. (b) Bias dependence of the on/off ratios measured on the two samples with and without the WS_2 layer.[159] (c) Molecular structures and schematic diagram of $MAPbI_3$/C8BTBT hybrid PDs. (d) Responsivity of $MAPbI_3$ and $MAPbI_3$/C8BTBT hybrid PDs as a function of the light wavelength.[167]

4.1.2. Organic materials

Organic semiconductors have been widely used in perovskite photodiodes as the hole/electron transport layer. Generally, the charge transport layers in perovskite photodiodes are used to modify the energy levels and reduce the dark currents.[24,90,168] Burn and co-workers demonstrated a low noise, IR-blind visible perovskite photodiode with performance metrics equivalent to commercially available silicon photodiodes.[24] The [6,6]-phenyl-C61-butyric acid methyl ester (PC60BM)/C60 cathode interlayer has three functions: (i) improving the diode temporal response; (ii) suppressing the dark current; and (iii) controlling the spectral response. Hence, the performance of the photodiode was greatly enhanced without compromising the LDR. Similarly, hole transport layers can also be employed to reduce the dark current and control the spectral response.[90]

Besides being charge transport layers in photodiodes, organic semiconductors are widely applied in photoconductors. PCBM was applied to perovskite hybrids in order to fabricate performance-enhanced photoconductors or phototransistors via enhancing the charge transfer.[169,170] Yang and co-workers fabricated a flexible and air-stable perovskite photoconductor based on the $MAPbI_3$/dioctylbenzothieno [2,3-b] benzothiophene (C8BTBT) bulk heterojunction;[167] the schematic device structure is exhibited in Fig. 9(c). The organic semiconductor C8BTBT has been fabricated via a simple, one-step solution process. Compared with pure $MAPbI_3$, the responsivity of hybrid-structure PDs was promoted by almost one order of magnitude (Fig. 9(d)). Furthermore, the hybrid-structure PDs held unique advantages of stability and flexibility. Due to the incorporation of C8BTBT, 70% of the original performance could be maintained after exposure to ambient conditions for 50 days without any encapsulation, and the photocurrent exhibited a decrease of less than 5% as the devices were bent for 10000 cycles at a small radius of 7.5 mm. In addition, poly(diketopyrrolopyrrole-terthiophene) (PDPP3T)[171] and rhodamine B[172] were also applied in hybrid-structure flexible perovskite PDs.

4.1.3. Metal oxides

Metal oxides have been widely applied in perovskite optoelectronic devices as charge transport layers due to their suitable energy levels and high mobility.[21,173] Metal oxides can also be applied in perovskite PDs for the follow-

ing reasons: (i) providing a mesoporous scaffold for perovskites; (ii) providing a high efficient charge transfer layer; (iii) band gap engineering; (iv) providing surface passivation; and (v) providing a blocking layer to reduce the dark current. Mesoporous TiO_2 was not only applied in perovskite to provide a mesoporous scaffold for perovskites, but also in perovskite photodiodes. Tress and co-workers fabricated high-gain, low-voltage $MAPbI_3$ PDs based on FTO/TiO_2 MP scaffold/$MAPbI_3$/Spiro-MeOTAD HTM/Au (FTO: fluorine-doped tin oxide; MP: mesoporous; HTM: hole transporting material), which showed the highest responsivity of 208 $A{\cdot}W^{-1}$ under 550 nm illumination.[174] Wang and co-workers reported a self-powered, UV–vis perovskite PD based on TiO_2 nanorods/$MAPbI_3$.[41] The TiO_2 in PDs not only provided a mesoporous scaffold for perovskites as mesoporous TiO_2, but also fitted the energy level alignment. In addition, ZnO nanorods[175–178] also provided a mesoporous scaffold for perovskites. Zhang and coworkers reported an inorganic perovskite–ZnO heterostructure perovskite photoconductor.[35] Owing to the interfacial charge transfer from perovskite to the ZnO layer, the responsivity and detectivity were largely enhanced. Additionally, flexible PDs based on $CsPbBr_3$/ZnO demonstrated excellent stability and outstanding flexibility. TiO_2 in the perovskite mentioned above[168] also matched the energy levels of ITO and PCBM, and enhanced the charge transfer efficiency. Choy and co-workers introduced a room temperature solution-processed NiO_x:PbI_2 hole transport layer into $MAPbI_3$ perovskite-based PDs.[179] The NiO_x:PbI_2 layer passivated the surface of the perovskite, and offered a large electron injection barrier at the ITO interface for suppressing dark current. Besides, the favorable energy level alignment with perovskite film also enhanced the hole extraction. Metal oxides can also act as a blocking layer in the perovskite photodiode. The dark current can be suppressed by adding an Al_2O_3 layer.[33]

Recently, amorphous indium gallium zinc oxide (IGZO) has become an attractive channel material for organic–inorganic hybrid phototransistors.[180] The advantageous features of IGZO, such as high field-effect carrier mobility and low-temperature large-area processing capabilities, make it possible to apply it in perovskite transistors. With an optical bandgap of about 3 eV, amorphous IGZO is ready to sense ultraviolet light with wavelengths shorter than 420 nm. Zhou and co-workers developed a hybrid phototransistor where IGZO was capped with a solution-processed perovskite layer.[181] The device structure of the hybrid phototransistor is depicted in Fig. 10(a). To obtain a low dark current, the morphology of the perovskite layer is prepared to be a needle-like film rather than a smooth, compact perovskite thin film. Although the responsivity and detectivity of IGZO transistors were relatively higher than that of the $MAPbI_3$-capped IGZO transistors, the latter were highly sensitive to light in both UV and visible regions (Fig. 10(b)). Since the IGZO layer is usually very thin, it introduces a new way for fabricating flexible perovskite phototransistors.

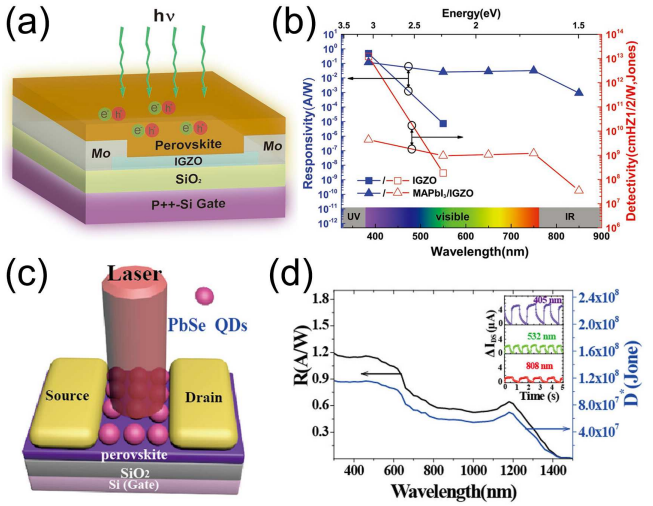


Fig. 10. (a) Schematic of $MAPbI_3$/IGZO hybrid phototransistors. (b) Responsivities of IGZO transistors and $MAPbI_3$/IGZO phototransistors at $V_{GS} = -10$ V.[181] (c) Schematic of perovskite/PbSe hybrid PD. (d) Responsivity and detectivity of the device as a function of the wavelength ranging from 300 nm to 1500 nm at bias voltage $V_{DS} = 2$ V and drain source voltage $V_{GS} = 0$ V.[46]

4.1.4. Quantum dots

The perovskite quantum dots have been discussed above; however, there are various materials that can be processed into CQDs, such as graphene, PbS, PbSe, HgTe, and CdSe/ZnS. They have been widely applied in PDs due to their ability to limit spectral absorption and offering a wide range of bandgaps.[32,127,128,182–184] It is advisable to combine the perovskite with CQDs of other materials to enhance the performance of PDs. Gong and co-workers fabricated $MAPbI_3$/PbS QDs hybrid perovskite photodiodes, in which PbS QDs induced an additional trap-state onto the surface of the $MAPbI_3$ film, thus forming ohmic contact at the $MAPbI_3$/aluminum (Al) interface.[185] As a result, the photodiodes based on hybrid perovskite achieved an EQE of $\sim 4500\%$, a responsivity of ~ 15 $A{\cdot}W^{-1}$, and a detectivity of over 6×10^{13} Jones at a small bias of 2 V. Zhang and co-workers demonstrated a transistor based on the $MAPbI_3$ perovskite/PbSe CQD heterostructure.[46] The architecture of the phototransistor is shown in Fig. 10(c). The perovskite thin film with a PbSe quantum dot active channel was made by a two-step spin-coating method. PbSe CQDs have a significant absorption capacity for near infrared (NIR) and short-wavelength light, which cannot be accessed by perovskites. Thus, the phototransistor exhibits a wide spectral response ranging from 300 nm to 1500 nm and relatively high responsivity (Fig. 10(d)). In addition, Yang and co-workers blended ternary PbS_xSe_{1-x} quantum dots with $MAPbBr_3$ quantum

dots to fabricate broadband photodiodes.[186] The photodiodes ITO/ZnO/$PbS_{0.4}Se_{0.6}$:$MAPbBr_3$/Au exhibit a maximum responsivity and specific detectivity of 21.48 $A{\cdot}W^{-1}$ and 3.59×10^{13} Jones, and 22.16 $A{\cdot}W^{-1}$ and 3.70×10^{13} Jones at room temperature under a 532 nm laser (49.8 $\mu W{\cdot}cm^{-2}$) and 980 nm laser (62 $\mu W{\cdot}cm^{-2}$), respectively.

4.2. Interface/band gap engineering

Layers are stacked together in a vertical perovskite device, producing several interfaces and interfacial regions. Hence, the interfaces and band alignment have significant influences on the charge processes in addition to the qualities of the layers themselves. As a result, interface engineering and band alignment engineering have become effective ways to promote the performance of perovskite PDs, especially the photodiodes.

Sargent and co-workers produced a thin, pinhole-free compact layer of Al_2O_3 on the nanostructured TiO_2 to passivate the surface trap states, and further added a thin layer of PCBM to minimize the dark current.[33] Zhang and co-workers introduced interface engineering to improve the responsivity and response speed of the perovskite photodiode by replacing the TiO_2 transport layer with a SnO_2 layer, and reduced the dark current by adding an inter-layer of poly(vinylpyrrolidone) between the electron transport layer and perovskite layer. The SnO_2 layer has a lower conduction band and lower trap density when compared with TiO_2 layer, thus leading to a better band alignment and a more efficient carrier transport.[34] Besides, organic semiconductors and 2D materials were also involved in the interface/band gap engineering of perovskite PDs. Huang and co-workers fabricated high-performance perovskite PDs with ingenious device design, in which the 4,4′-bis[(p-trichlorosilylpropylphenyl)phenylamino]-biphenyl (TPD–Si_2) serves as the hole transporting/electron blocking layer (Fig. 11(a)).[31] There are abundant defects/traps on the surface of perovskite, which are detrimental to the performance of photovoltaic devices. However, it is possible to exploit traps to boost the performance of perovskite PDs. When introducing an electron transport layer between ITO and the perovskite layer, the ITO/BCP(C60)/$MAPbI_3$/MoO_3/Ag device showed photovoltaic *I*–*V* curves. Whereas, benefiting from the trapped hole-induced electron injection, the $MAPbI_3$ PD (device shown in Fig. 11(a)) worked as a photodiode in the dark and showed a large photoconductive gain of ~ 489 at a very low driving voltage of -1 V under illumination. Thus, the photocurrent of $MAPbI_3$ PD was more than 100 times larger than that of the reference photovoltaic device (Fig. 11(b)). For the $MAPbI_3$ PD, there were large energy barriers for carriers injecting into the perovskite layer, which explained the rectification behavior in the dark. However, when the device was illuminated, one type of trapped charge in the $MAPbI_3$ active layer induced band bending in the perovskite layer close to one of the electrodes. Thus, the Schottky junction thickness was reduced, which allowed the injection of the opposite charges under reverse bias (Fig. 11(c)). This work also provided a novel approach to introduce the photoconductive effect to a vertical PD by interface/band gap engineering.

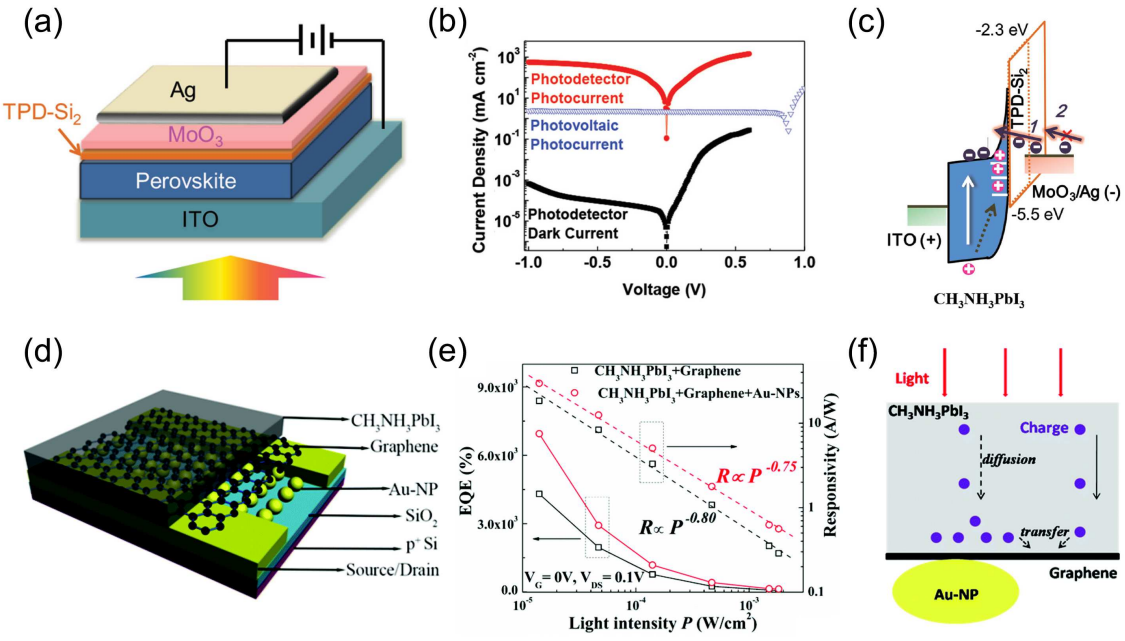


Fig. 11. (a) Device structure of the $MAPbI_3$ PD. (b) Photocurrent and dark current of the $MAPbI_3$, and the photocurrent of the reference photovoltaic device, which has a structure of ITO/PEDOT:PSS/$MAPbI_3$/PCBM/C60/BCP/Al. (c) Energy diagram of the $MAPbI_3$ PD at reverse bias under illumination.[31] (d) Device structure of perovskite–graphene hybrid PDs. (e) The responsivity and EQE versus light intensity relationships for the graphene–perovskite and graphene–perovskite–gold nanoparticle (Au-NP) devices. (f) Schematic of generation, diffusion, and transfer of photo-induced carriers in the perovskite layer with and without the influence of Au-NPs.[37]

Sum and co-workers introduced a vacancy-engineered MoS_2 monolayer to achieve ultrafast hole transfer at the interface of MoS_2 and perovskite.[187] It was found that creating S vacancies in MoS_2 strongly improves the hole transfer rate between $MAPbI_3$ and MoS_2 layers. Importantly, this work highlights the feasibility of applying defect engineering in tuning the band alignment of 2D transition metal dichalcogenides (TMDCs)–perovskite hybrid PDs. Sun and co-workers inserted Au-NPs into $MAPbI_3$/graphene hybrid PDs to achieve a significant responsivity enhancement.[37] The schematic of the device structure is illustrated in Fig. 11(d). Au-NPs were bonded on the Si/SiO_2 substrate with a Au source and drain electrodes through a self-assembled monolayer of 3-aminopropyl-triethoxysilane. The responsivity and EQE of the $MAPbI_3$–graphene–Au-NP hybrid PD (P–G–Au PD) are almost two times higher than those of the device without Au-NPs (Fig. 11(e)). The responsivity decreased with illumination intensity due to the increased probability of carrier recombination as the carrier density increases. For P–G–Au PDs, most photo-induced carriers were generated around the interface between graphene and perovskite due to the near-field enhancement of Au-NPs. Thus, the recombination of photon-generated carriers was smaller than that of carriers generated far from this interface (Fig. 11(f)). As a result, the carrier extraction efficiency and response speed were improved, which demonstrated a promising strategy to improve the performance of graphene-based PDs.

4.3. Flexible PDs

Flexible PDs have been widely applied in wearable devices, stretchable displays, and electronic skins due to their reduced cost and light weight.[188–190] Fortunately, perovskites can be prepared by solution processing, which renders the possibility for them to be assembled into flexible PDs. In addition to the perovskite itself being compatible with flexible PDs, we have discussed several strategies to fabricate a flexible PD based on perovskites, including reducing the dimensions of bulk perovskite and integrating them with 2D materials and organic semiconductors. As we mentioned in Section 3.1, Xie and co-workers first demonstrated the flexible perovskite PD through a low-cost, solution-processed, and self-assembly strategy on an ITO/PET substrate.[47] The device exhibited high sensitivity and fast response speed. Importantly, the photocurrent remained nearly unchanged under different bending states or 120 cycles of bending, which indicated the extreme flexibility, good folding endurance, and electrical stability of the device. In addition, similar flexible PDs based on pure perovskite polycrystalline film can also be processed by a vapor–solution method.[84] Besides thin film, there are other forms of pure perovskites that can be applied in flexible devices, such as nanowires, networks, nanosheets, and nanoflakes.[118,143,146] Song and co-workers reported flexible PD arrays based on uniform perovskite networks synthesized on PET by controlling the crystallization.[118] The uniform intersecting ribbon-like crystal network (Fig. 12(a) and inset) demonstrated good uniformity and transparency compared to thin films and nanowires, combining the advantages of thin films and nanowires. Figure 12(b) shows the schematic diagram of the individual device structure (top) and network PD array (bottom). The poly(methyl methacrylate) (PMMA) layer was deposited to form a sandwich structure (PET/perovskite/PMMA), which greatly improved the device stability so that the network PD arrays could be easily kept intact for one month of storage in air. The photocurrent shrank less than 10% after 10000 bending cycles at a fixed angle of 40° (Fig. 12(c)), which indicated superior flexibility and stability of the devices.

For hybrid perovskite flexible PDs, the perovskite was usually hybridized with organic semiconductors, such as C8BTBT, PDPP3T, PCBM, single-walled carbon nanotubes (SCNTs), and rhodamine B.[167,171,172,191,192] Shi and co-workers reported a flexible broad-band PD based on a bilayer composite film of $MAPbI_3$/PDPP3T.[171] The fabrication process is illustrated in Fig. 12(d). Perovskite and PDPP3T solutions were successively dropped onto the PET substrate with interdigitated gold electrodes. Since PDPP3T is a narrow band gap-conjugated polymer, the absorption spectrum of the pristine PDPP3T has a dominant band centered at 838 nm and a slightly weaker shoulder band with a peak at 763 nm located outside the spectral coverage of the $MAPbI_3$ absorber (Fig. 12(e)). However, the $MAPbI_3$/PDPP3T hybrid film has complementary absorption in the 550–940 nm region, so it is promising for the fabrication of a UV–vis–NIR PD. Hence, the responsivity of the flexible hybrid PD was significantly enhanced. The responsivity of the hybrid PD at 650 nm or 835 nm was measured to be 90% or 85% after 1000 cycles of bending/straightening to a curvature radius of 7 mm (Figs. 12(f) and 12(g)). Huang and co-workers fabricated a flexible $MAPbCl_3$/SCNT hybrid PD,[191] which presented a high responsivity (2×10^5 $A \cdot W^{-1}$) to UV light at an intensity of 1 $\mu W \cdot cm^{-2}$, and almost no response to visible light. Combined with the comparable electrical and photosensitive properties of the $MAPbBr_3$/SCNT hybrid PD, a series of flexible devices applied to distinguish UV, visible, and IR spectra were attained. In addition, several materials mentioned in Section 4.1 were also compatible with the flexible devices, and low-dimension materials as well as soft organic semiconductors would be good choices for fabricating a flexible hybrid PD.

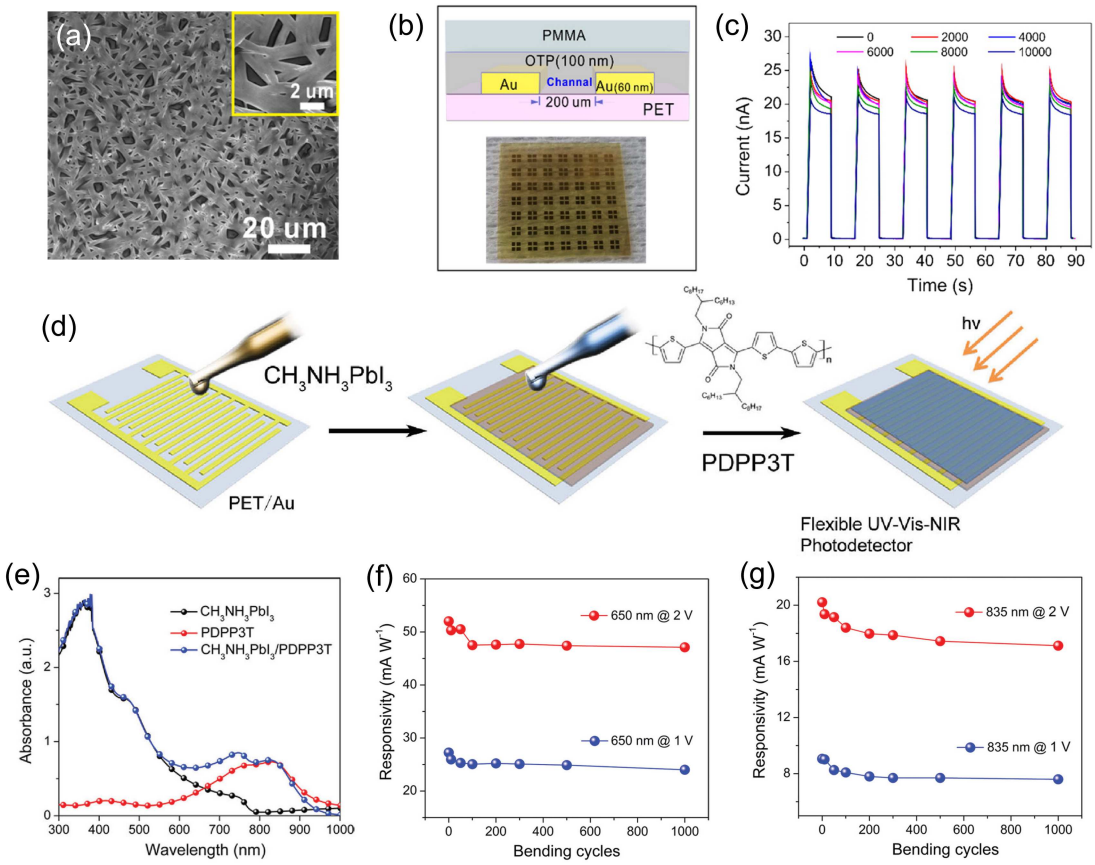


Fig. 12. (a) Morphologies of perovskite crystals networks. (b) Schematic of a PD (top), and photograph of network PD arrays (bottom). (c) *I*–*t* curve evolution at different bending cycles (0–10000 times) at a fixed angle of 40°.[118] (d) Schematic illustration of fabricating the flexible $MAPbI_3$/PDPP3T PD. (e) UV–vis–IR absorption spectra of $MAPbI_3$ and $MAPbI_3$/PDPP3T composite films. (f) Responsivity versus bending cycle number at a radius of 7 mm under 650 nm and (g) 835 nm.[171]

4.4. Narrowband PDs

Narrowband PDs used for spectrally selective photodetection are widely required in imaging. Spectral discrimination in state-of-the-art narrowband PDs is usually realized by one of several approaches: (i) by combining broadband PDs with bandpass filters,[193] (ii) by using photoactive materials with narrowband absorption,[194] (iii) by intentionally enhancing absorption in a particular wavelength range via the plasmonic effect,[195] and (iv) by splitting the light into its component colors.[196] Perovskites have good prospects for application in narrowband PDs due to the controllable band gap, large carrier diffusion length, and large absorption coefficient. These unique properties also extend the strategies to carry out the device engineering for narrowband perovskite PDs.

The vertical PDs based on single-crystal perovskite are well suited for narrowband PDs, which has been discussed in Section 3.2. Meredith and co-workers reported red, green, and blue filterless narrowband visible photodiodes, all with a FWHM of < 100 nm.[101] The working principle of narrowband PDs was a charge collection narrowing (CCN) mechanism, which had been discussed in detail by Burn and co-workers.[197] The photodiode architecture is shown in Fig. 13(a) and inset, in which a photoactive layer (perovskite) is sandwiched between a transparent anode (ITO/PEDOT:PSS) and cathode stack (C60/LiF/Ag). The CCN is realized because the junction has a high optical density and long transit time for photogenerated carrier extraction. There are three different absorption regimes: high α, where the incident light intensity falls off exponentially within the junction (the Beer–Lambert regime); low α, where the incident light propagates within the junction and is subject to interference (the cavity regime); and $\alpha = 0$, where the incident light is almost not absorbed. Considering that the surface-generated carriers will be subject to significant recombination losses due to the higher local carrier concentration and imbalanced transit times for the electrons and holes, the charge collection efficiency will be suppressed and result in a low EQE in the Beer–Lambert regime. Figure 13(b) shows the optical field distributions in the red narrowband photodiodes for four wavelengths, in which the $\lambda < 600$ nm photons cannot penetrate the whole film, carriers are surface-generated, and the 600 nm $< \lambda <$ 700 nm photons can penetrate the film and photocarriers are volume-generated. In addition, the narrowband response can be pushed out into the NIR, and the FWHM can be tuned further (from $\sim$ 40 nm to 200 nm) by changing the halide ratio (Fig. 13(c)). The CCN principle has been widely applied to fabricate narrowband perovskites.[36,198] In

particular, Bakr and co-workers fabricated a PD operating in both broadband (upon bottom illumination) and narrowband regimes (upon top illumination), which was realized due to the combined effect of CCN and a surface-located polycrystalline film.[19]

Based on the common practice of combining broadband PDs with bandpass filters to achieve narrowband detection, Huang and co-workers demonstrated a new method to tune the spectral response band of perovskite PDs with perovskite filters.[199] They prepared two types of devices, the working principle schematic diagram of which is exhibited in Fig. 13(d). The perovskite photodiode with a thick active layer operates based on using the same material as both the filter and active layer. The perovskite photodiode combining a thick perovskite layer as an optical filter in front of light incident window operates based on the common practice of combining broadband PDs with bandpass filters, in which the long wavelength light is filtered by the perovskite-1 layer. The schematic device structures of two types of narrowband perovskite PDs are shown in Fig. 13(e), in which the perovskite-1 layer denotes $MAPbBr_{3-x}I_x$, and the perovskite-2 layer denotes neat $MAPbI_3$. The EQE spectrum shows that using mixed-halide perovskites as the perovskite-1 layer is more efficient than using neat $MAPbI_3$ as both the filter and active layer (Fig. 13(f)). In a similar way, the perovskite can also be applied in narrowband PDs based on non-perovskite material as a filter layer.[200]

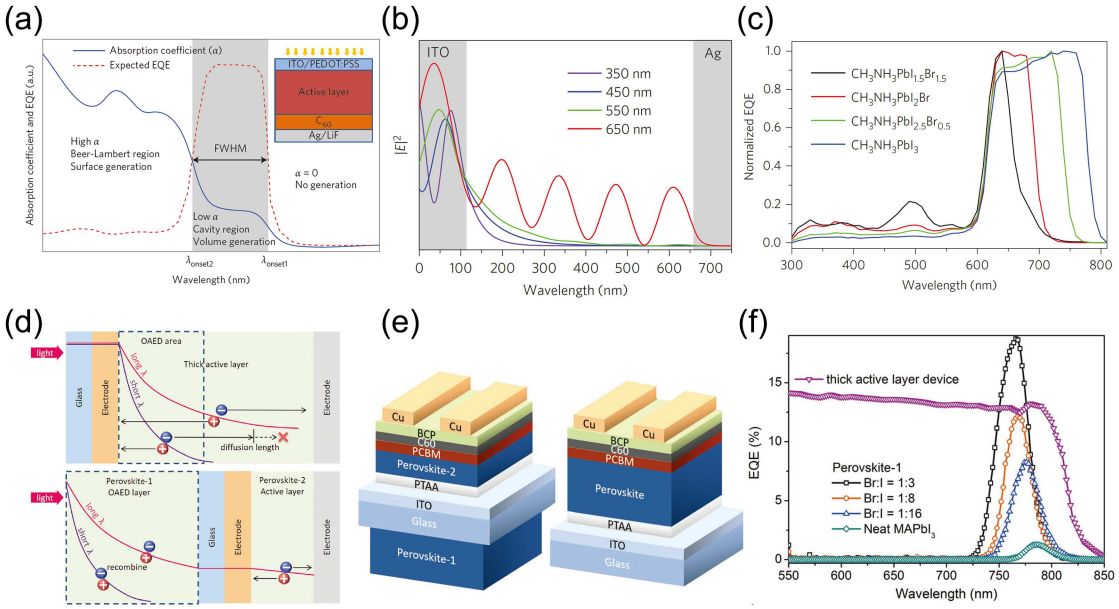


Fig. 13. (a) Schematic of the working principles of CCN photodiodes. (b) Working mechanism and performance of the red narrowband CCN photodiodes. (c) EQEs at −0.5 V of the red narrowband photodiodes fabricated with different ratios of PbI_2 and $PbBr_2$.[101] (d) Schematic showing a narrowband PD with a thick active layer and integrated perovskite layer. (e) Device structures of narrowband PDs with an integrated perovskite layer (left) and thick active layer (right). (f) EQE spectra of devices with a thick active layer and devices with an integrated perovskite-1 filter layer with different mixed-halides ratios.[199]

5. Conclusion and perspectives

In summary, we introduce and discuss perovskite PDs in terms of chemical compositions, material morphologies, device architectures, and engineering strategies. The use of perovskites in PDs is compelling due to their unique electric and optical properties, simple and low-cost processing, and mechanical flexibility. There have been various strategies for synthesizing perovskites, such as solution processing, the EISA method, and chemical vapor deposition. Several types of perovskite materials for PDs have been demonstrated, including polycrystalline films, single crystals, nanowires/nanorods, quantum dots/nanocrystals, and 2D/quasi-2D perovskites. PDs based on various perovskite materials possess very different merits regarding photoelectric performance. The key parameters of perovskite PDs are listed and compared in Table 2. Polycrystalline films are most widely used because they are easy to fabricate by solution methods and are compatible with different PD configurations. However, vast trap sites that exist in the grain boundary and interface limit the performance of PDs, which get a valid settlement by the single-crystal and low-dimensional perovskites such as nanowires, nanoplates, and nanosheets. In particular, perovskite single crystals and nanocrystal/quantum dots are appropriate for narrow-band PDs and flexible PDs, respectively. Perovskites with novel morphology were also reported to improve the performance of PDs. Single-crystalline layered perovskite nanowires are fabricated, in which insulating organic cations and conductive inorganic frameworks are self-organized layer-by-layer along the nanowire length.[201] This creates high resistance in the interior of the crystals and high conductivity at the edges of the crystals. The ultra-

high responsivity ($> 1.5 \times 10^4$ A·W^{-1}) and detectivity ($> 7 \times 10^{15}$ Jones) of the PD originate from a combination of efficient free-carrier edge conduction and resistive hopping barriers in the layered perovskites. A new inorganic perovskite film via a vapor deposition method using a dual-phase inorganic material ($CsPbBr_3$–$CsPb_2Br_5$ mixed phases) was proposed to further improve the quality of perovskites.[202] The $CsPb_2Br_5$ provided self-passivation, which was similar to the PbX_2 passivation in the hybrid perovskite.[11,203] Thus, the recombination of the charge carriers was reduced, and the stability of the inorganic perovskite was enhanced. Other processing methods such as spray-coating, ink-jet printing, and electrospinning may also have great prospects in fabricating perovskites.[190,204,205]

In terms of the device engineering of perovskite PDs, the core issues are different for the three types of PDs (photodiodes, photoconductors, and phototransistors). For perovskite photodiodes, the universal strategies to enhance the performance were introducing an interlayer to regulate the energy band and passivate the traps on the interface, which could suppress the dark current and boost the photocurrent. For perovskite photoconductors, it is pivotal to increase the gain of the device. According to Eq. (4) in Section 2.1.1, the gain G of PDs is determined by the excess minority carrier lifetime τ, channel length L, and the carrier mobility of the active layer μ. In consequence, low-dimensional perovskites possess advantages due to their small size, which means a smaller channel length. The carrier lifetime τ can be prolonged by hybridizing perovskite with materials that possess shallow defects, which could trap one type of the photogenerated carriers.[27] Meanwhile, perovskite phototransistors are engineered based on photoconductors. Generally, graphene was applied to enhance the performance of perovskite phototransistors.[45,138,158] The gain of the phototransistor can be remarkably increased by the photogating effect, which arises from the graphene–perovskite interface.[45] TDMs are also promising to be widely applied in hybrid perovskite phototransistors due to their similar electrical and mechanical properties.[161] In addition, h-BN was also adopted to be a substrate preserving the intrinsically high mobility of graphene,[162] or as an effective protection for perovskite to significantly extend the lifetime of the device.[206] Although impressive advances have been achieved by the various device engineering strategies discussed above, there are still several shortcomings that limit the development of perovskite PDs. (i) These PDs are usually operated at a high bias voltage, which leads to a large dark current and limits the detectivity of devices. The dark current can be suppressed by an interlayer or interfacial modification. In addition, self-powered perovskite PDs also facilitate application of the PDs at a low driving voltage or in a weak light.[39,207–210] (ii) Because of the wide energy band gap of Pb-based perovskites, most perovskite PDs usually have weak responsivity to NIR light. By replacing Pb with Sn or alloying the materials with Sn, absorption in the NIR range can be enhanced.[211–214] However, the structure of perovskites is ruined in air due to the easy oxidation of Sn^{2+} to Sn^{4+}. To enlarge the response of the PDs in the NIR range, a broadband PD based on the $MAPbI_3$/PbSe quantum dot heterojunction that has a wide spectral response spectrum ranging from 300 nm to 1500 nm was fabricated.[46] In addition, recent research revealed that upconversion[215,216] and two-photon absorption[217] contributed to the response in the NIR region. (iii) The instability problem has yet to be solved. On the one hand, perovskites with mixing of MA^+, FA^+, and Cs^+ are shown to be more thermally and structurally stable than the pure perovskites.[62,63] On the other hand, the 2D perovskites have been reported to have a better moisture stability than 3D perovskites;[74,148] recent studies on perovskite solar cells also revealed that 2D/3D perovskite compounds showed outstanding thermal and moisture stability.[218–220] These results are beneficial to guiding the processing of perovskites with long-term stability. (iv) The toxicity of Pb-based perovskites is still hard to overcome because Pb is indispensable for achieving high performance in perovskite optoelectronics. Although great effort has been made in Pb-free perovskite photovoltaics,[66] there is still a long way to go to apply the lead-free perovskites to PDs and improve the photoelectric conversion efficiency of Pb-free perovskite optoelectronics. Above all, additional research efforts should be focused on fully understanding the properties and resolving the aforementioned bottlenecks in order to promote the performance of future devices.

References

[1] Baeg K J, Binda M, Natali D, Caironi M and Noh Y Y 2013 *Adv. Mater.* **25** 4267

[2] Konstantatos G, Clifford J, Levina L and Sargent E H 2007 *Nat. Photon.* **1** 531

[3] Konstantatos G and Sargent E H 2010 *Nat. Nanotechnol.* **5** 391

[4] Konstantatos G, Howard I, Fischer A, Hoogland S, Clifford J, Klem E, Levina L and Sargent E H 2006 *Nature* **442** 180

[5] García De Arquer F P, Armin A, Meredith P and Sargent E H 2017 *Nat. Rev. Mater.* **2** 16100

[6] Takahashi Y, Hasegawa H, Takahashi Y and Inabe T 2013 *J. Solid State Chem.* **205** 39

[7] Stranks S D, Eperon G E, Grancini G, Menelaou C, Alcocer M J P, Leijtens T, Herz L M, Petrozza A and Snaith H J 2013 *Science* **342** 341

[8] Xing G, Mathews N, Sun S, Lim S S, Lam Y M, Graťzel M, Mhaisalkar S and Sum T C 2013 *Science* **342** 344

[9] Ponseca C S, Savenije T J, Abdellah M, Zheng K, Yartsev A, Pascher T, Harlang T, Chabera P, Pullerits T, Stepanov A, Wolf J P and Sundström V 2014 *J. Am. Chem. Soc.* **136** 5189

[10] De Wolf S, Holovsky J, Moon S J, Löper P, Niesen B, Ledinsky M, Haug F J, Yum J H and Ballif C 2014 *J. Phys. Chem. Lett.* **5** 1035

[11] Jiang Q, Chu Z, Wang P, Yang X, Liu H, Wang Y, Yin Z, Wu J, Zhang X and You J 2017 *Adv. Mater.* **29** 1703852

[12] Tan H, Jain A, Voznyy O, Lan X, De Arquer F P G, Fan J Z, Quintero-Bermudez R, Yuan M, Zhang B, Zhao Y, Fan F, Li P, Quan L N, Zhao Y, Lu Z H, Yang Z, Hoogland S and Sargent E H 2017 *Science* **355** 722

[13] Heo J H, Im S H, Noh J H, Mandal T N, Lim C S , Chang J A, Lee Y H, Kim H, Sarkar A, Nazeeruddin M K, Grätzel M and Seok S I 2013 *Nat. Photon.* **7** 486

[14] Zhou H, Chen Q, Li G, Luo S, Song T B, Duan H S, Hong Z, You J, Liu Y and Yang Y 2014 *Science* **345** 542

[15] Kojima A, Teshima K, Shirai Y and Miyasaka T 2009 *J. Am. Chem. Soc.* **131** 6050

[16] N R E L, efficiency chart, https://www.nrel.gov/pv/assets/images/efficiency-chart-20180716.jpg [2018-10-17]

[17] Ting H K, Ni L, Ma S B, Ma Y Z, Xiao L X and Chen Z J 2015 *Acta Phys. Sin.* **64** 038802 (in Chinese)

[18] Song Z H, Wang S R, Xiao Y and Li X G 2015 *Acta Phys. Sin.* **64** 033301 (in Chinese)

[19] Saidaminov M I, Haque M A, Savoie M, Abdelhady A L, Cho N, Dursun I, Buttner U, Alarousu E, Wu T and Bakr O M 2016 *Adv. Mater.* **28** 8144

[20] Zhang L et al 2017 *Nat. Commun.* **8** 15640

[21] Tan Z K et al 2014 *Nat. Nanotechnol.* **9** 687

[22] Xing G, Mathews N, Lim S S, Yantara N, Liu X, Sabba D, Grätzel M, Mhaisalkar S and Sum T C 2014 *Nat. Mater.* **13** 476

[23] Zhu H, Fu Y, Meng F, Wu X, Gong Z, Ding Q, Gustafsson M V, Trinh M T, Jin S and Zhu X Y 2015 *Nat. Mater.* **14** 636

[24] Lin Q, Armin A, Lyons D M, Burn P L and Meredith P 2015 *Adv. Mater.* **27** 2060

[25] Li F, Ma C, Wang H, Hu W J, Yu W L, Sheikh A D and Wu T 2015 *Nat. Commun.* **6** 8238

[26] Saleh B E A and Teich M C 2007 *Fundamentals Photonics* (2nd Edn.) (New Jersey: Wiley) pp. 755

[27] Fang H and Hu W 2017 *Adv. Sci.* **4** 1700323

[28] Li X, Gao C, Duan H, Lu B, Wang Y, Chen L, Zhang Z, Pan X and Xie E 2013 *Small* **9** 2005

[29] Guo F, Yang B, Yuan Y, Xiao Z, Dong Q, Bi Y and Huang J 2012 *Nat. Nanotechnol.* **7** 798

[30] Saidaminov M I, Adinolfi V, Comin R, Abdelhady A L, Peng W, Dursun I, Yuan M, Hoogland S, Sargent E H and Bakr O M 2015 *Nat. Commun.* **6** 8724

[31] Dong R, Fang Y, Chae J, Dai J, Xiao Z, Dong Q, Yuan Y, Centrone A, Zeng X C and Huang J 2015 *Adv. Mater.* **27** 1912

[32] Ren Z, Sun J, Li H, Mao P, Wei Y, Zhong X, Hu J, Yang S and Wang J 2017 *Adv. Mater.* **29** 1702055

[33] Sutherland B R, Johnston A K, Ip A H, Xu J, Adinolfi V, Kanjanaboos P and Sargent E H 2015 *ACS Photon.* **2** 1117

[34] Wang Y, Zhang X W, Jiang Q, Liu H, Wang D G, Meng J H, You J B and Yin Z G 2018 *ACS Appl. Mater. Interfaces* **10** 6505

[35] Liu H, Zhang X, Zhang L, Yin Z, Wang D, Meng J, Jiang Q, Wang Y and You J 2017 *J. Mater. Chem. C* **5** 6115

[36] Fang Y, Dong Q, Shao Y, Yuan Y and Huang J 2015 *Nat. Photon.* **9** 679

[37] Sun Z, Aigouy L and Chen Z 2016 *Nanoscale* **8** 7377

[38] Dou L, Yang Y M, You J, Hong Z, Chang W H, Li G and Yang Y 2014 *Nat. Commun.* **5** 5404

[39] Lu H, Tian W, Cao F, Ma Y, Gu B and Li L 2016 *Adv. Funct. Mater.* **26** 1296

[40] Tong G, Geng X, Yu Y, Yu L, Xu J, Jiang Y, Sheng Y, Shi Y and Chen K 2017 *RSC Adv.* **7** 18224

[41] Zhou H, Song Z, Tao P, Lei H, Gui P, Mei J, Wang H and Fang G 2016 *RSC Adv.* **6** 6205

[42] Shen L, Fang Y J, Wang D, Bai Y, Deng Y H, Wang M M, Lu Y F and Huang J S 2016 *Adv. Mater.* **28** 10794

[43] Liu Y C, Sun J K, Yang Z, Yang D, Ren X D, Xu H, Yang Z P and Liu S Z 2016 *Adv. Opt. Mater.* **4** 1829

[44] Cao F, Yu D, Li X, Zhu Y, Sun Z, Shen Y, Wei Y, Wu Y and Zeng H 2017 *J. Mater. Chem. C* **5** 7441

[45] Lee Y, Kwon J, Hwang E, Ra C H, Yoo W J, Ahn J H, Park J H and Cho J H 2015 *Adv. Mater.* **27** 41

[46] Yu Y et al 2017 *J. Phys. Chem. Lett.* **8** 445

[47] Hu X, Zhang X, Liang L, Bao J, Li S, Yang W and Xie Y 2014 *Adv. Funct. Mater.* **24** 7373

[48] Maculan G, Sheikh A D, Abdelhady A L, Saidaminov M I, Haque M A, Murali B, Alarousu E, Mohammed O F, Wu T and Bakr O M 2015 *J. Phys. Chem. Lett.* **6** 3781

[49] Li C, Lu X, Ding W, Feng L, Gao Y and Guo Z 2008 *Acta Crystallogr. Sect. B: Struct. Sci.* **64** 702

[50] Kieslich G, Sun S and Cheetham A K 2014 *Chem. Sci.* **5** 4712

[51] Sun Q and Yin W J 2017 *J. Am. Chem. Soc.* **139** 14905

[52] Seok S I, Grätzel M and Park N G 2018 *Small* **14** 1704177

[53] Xiao Z and Yan Y 2017 *Adv. Energy Mater.* **7** 1701136

[54] Calvo M E 2017 *J. Mater. Chem. A* **5** 20561

[55] Conings B et al 2015 *Adv. Energy Mater.* **5** 1500477

[56] Pearson A J, Eperon G E, Hopkinson P E, Habisreutinger S N, Wang J T W, Snaith H J and Greenham N C 2016 *Adv. Energy Mater.* **6** 1600014

[57] Wang Z, McMeekin D P, Sakai N, van Reenen S, Wojciechowski K, Patel J B, Johnston M B and Snaith H J 2017 *Adv. Mater.* **29** 1604186

[58] Zhang Y Y, Chen S, Xu P, Xiang H, Gong X G, Walsh A and Wei S H 2018 *Chin. Phys. Lett.* **35** 036104

[59] McMeekin D P et al 2016 *Science* **351** 151

[60] Jeon N J, Noh J H, Yang W S, Kim Y C, Ryu S, Seo J and Seok S I 2015 *Nature* **517** 476

[61] Pellet N, Gao P, Gregori G, Yang T Y, Nazeeruddin M K, Maier J and Grätzel M 2014 *Angew. Chem. Int. Ed.* **53** 3151

[62] Lee J W, Kim D H, Kim H S, Seo S W, Cho S M and Park N G 2015 *Adv. Energy Mater.* **5** 1501310

[63] Yi C, Luo J, Meloni S, Boziki A, Ashari-Astani N, Grätzel C, Zakeeruddin S M, Röthlisberger U and Grätzel M 2016 *Energy Environ. Sci.* **9** 656

[64] Eperon G E, Stranks S D, Menelaou C, Johnston M B, Herz L M and Snaith H J 2014 *Energy Environ. Sci.* **7** 982

[65] Volonakis G, Filip M R, Haghighirad A A, Sakai N, Wenger B, Snaith H J and Giustino F 2016 *J. Phys. Chem. Lett.* **7** 1254

[66] Shi Z, Guo J, Chen Y, Li Q, Pan Y, Zhang H, Xia Y and Huang W 2017 *Adv. Mater.* **29** 1605005

[67] Zhao X G, Yang J H, Fu Y, Yang D, Xu Q, Yu L, Wei S H and Zhang L 2017 *J. Am. Chem. Soc.* **139** 2630

[68] Settanni G, Zhou J, Suo T, Schöttler S, Landfester K, Schmid F and Mailänder V 2015 *J. Mater. Chem. A* **3** 23829

[69] Hoye R L Z et al 2016 *Chem. Eur. J.* **22** 2605

[70] Cortecchia D, Dewi H A, Yin J, Bruno A, Chen S, Baikie T, Boix P P, Grätzel M, Mhaisalkar S, Soci C and Mathews N 2016 *Inorg. Chem.* **55** 1044

[71] Jagielski J, Kumar S, Yu W Y and Shih C J 2017 *J. Mater. Chem. C* **5** 5610

[72] Quan L N et al 2016 *J. Am. Chem. Soc.* **138** 2649

[73] Tsai H et al 2016 *Nature* **536** 312

[74] Smith I C, Hoke E T, Solis-Ibarra D, McGehee M D and Karunadasa H I 2014 *Angew. Chem. Int. Ed.* **53** 11232

[75] Sutherland B R and Sargent E H 2016 *Nat. Photon.* **10** 295

[76] Liu M, Johnston M B and Snaith H J 2013 *Nature* **501** 395

[77] Jeon N J, Noh J H, Kim Y C, Yang W S, Ryu S and Seok S I 2014 *Nat. Mater.* **13** 897

[78] Chen Q, Zhou H, Hong Z, Luo S, Duan H S, Wang H H, Liu Y, Li G and Yang Y 2014 *J. Am. Chem. Soc.* **136** 622

[79] Nie W et al 2015 *Science* **347** 522

[80] Bi D, Yi C, Luo J, Décoppet J D, Zhang F, Zakeeruddin S M, Li X, Hagfeldt A and Grätzel M 2016 *Nat. Energy* **1** 16142

[81] Li X, Bi D, Yi C, Décoppet J D, Luo J, Zakeeruddin S M, Hagfeldt A and Grätzel M 2016 *Science* **353** 58

[82] Lee J W, Kim H S and Park N G 2016 *Acc. Chem. Res.* **49** 311

[83] Zuo L, Dong S, De Marco N, Hsieh Y T, Bae S H, Sun P and Yang Y 2016 *J. Am. Chem. Soc.* **138** 15710

[84] Hu W et al 2017 *Adv. Mater.* **29** 1703256

[85] Guo Y, Liu C, Tanaka H and Nakamura E 2015 *J. Phys. Chem. Lett.* **6** 535

[86] Zhang Y, Du J, Wu X, Zhang G, Chu Y, Liu D, Zhao Y, Liang Z and Huang J 2015 *ACS Appl. Mater. Interfaces* **7** 21634

[87] Wang F, Mei J, Wang Y, Zhang L, Zhao H and Zhao D 2016 *ACS Appl. Mater. Interfaces* **8** 2840

[88] Wang Y, Yang D, Zhou X, Alshehri S M, Ahamad T, Vadim A and Ma D 2016 *J. Mater. Chem. C* **4** 7415

[89] Wang W et al 2017 *Adv. Funct. Mater.* **27** 1703953

[90] Fang Y and Huang J 2015 *Adv. Mater.* **27** 2804

[91] Cho N et al 2016 *Nat. Commun.* **7** 13407

[92] Saidaminov M I et al 2015 *Nat. Commun.* **6** 7586

[93] Liu Y et al 2015 *Adv. Mater.* **27** 5176

[94] Han Q F et al 2016 *Adv. Mater.* **28** 2253

[95] Dirin D N, Cherniukh I, Yakunin S, Shynkarenko Y and Kovalenko M V 2016 *Chem. Mater.* **28** 8470
[96] Shi D et al 2015 *Science* **347** 519
[97] Dong Q, Fang Y, Shao Y, Mulligan P, Qiu J, Cao L and Huang J 2015 *Science* **347** 967
[98] Lian Z, Yan Q, Lv Q, Wang Y, Liu L, Zhang L, Pan S, Li Q, Wang L and Sun J L 2015 *Sci. Rep.* **5** 16563
[99] Shamsi J, Abdelhady A L, Accornero S, Arciniegas M, Goldoni L, Kandada A R S, Petrozza A and Manna L 2016 *ACS Energy Lett.* **1** 1042
[100] Dang Y, Liu Y, Sun Y, Yuan D, Liu X, Lu W, Liu G, Xia H and Tao X 2015 *CrystEngComm* **17** 665
[101] Lin Q, Armin A, Burn P L and Meredith P 2015 *Nat. Photon.* **9** 687
[102] Liu Y et al 2018 *Adv. Mater.* **30** 1707314
[103] Adinolfi V, Ouellette O, Saidaminov M I, Walters G, Abdelhady A L, Bakr O M and Sargent E H 2016 *Adv. Mater.* **28** 7264
[104] Saidaminov M I et al 2017 *Adv. Opt. Mater.* **5** 1600704
[105] Shaikh P A, Shi D, Retamal J R D, Sheikh A D, Haque M A, Kang C F, He J H, Bakr O M and Wu T 2016 *J. Mater. Chem. C* **4** 8304
[106] Yakunin S, Dirin D N, Shynkarenko Y, Morad V, Cherniukh I, Nazarenko O, Kreil D, Nauser T and Kovalenko M V 2016 *Nat. Photon.* **10** 585
[107] Wei H et al 2016 *Nat. Photon.* **10** 333
[108] Zhang Y, Liu Y, Li Y, Yang Z and Liu S 2016 *J. Mater. Chem. C* **4** 9172
[109] Yao S and Zhu Y 2015 *Adv. Mater.* **27** 1480
[110] Gong S and Cheng W 2017 *Adv. Electron. Mater.* **3** 1600314
[111] Zhang D, Eaton S W, Yu Y, Dou L and Yang P 2015 *J. Am. Chem. Soc.* **137** 9230
[112] Tang X, Zu Z, Shao H, Hu W, Zhou M, Deng M, Chen W, Zang Z, Zhu T and Xue J 2016 *Nanoscale* **8** 15158
[113] Dong D, Deng H, Hu C, Song H, Qiao K, Yang X, Zhang J, Cai F, Tang J and Song H 2017 *Nanoscale* **9** 1567
[114] Horváth E, Spina M, Szekrényes Z, Kamarás K, Gaal R, Gachet D and Forró L 2014 *Nano Lett.* **14** 6761
[115] Spina M, Lehmann M, Náfrádi B, Bernard L, Bonvin E, Gaál R, Magrez A, Forrõ L and Horváth E 2015 *Small* **11** 4824
[116] Spina M, Náfrádi B, Tóháti H M, Kamarás K, Bonvin E, Gaal R, Forró L and Horváth E 2016 *Nanoscale* **8** 4888
[117] Spina M, Bonvin E, Sienkiewicz A, Forró L and Horváth E 2016 *Sci. Rep.* **6** 19834
[118] Deng H, Yang X, Dong D, Li B, Yang D, Yuan S, Qiao K, Cheng Y B, Tang J and Song H 2015 *Nano Lett.* **15** 7963
[119] Deng H et al 2015 *Nanoscale* **7** 4163
[120] Gao L et al 2016 *Nano Lett.* **16** 7446
[121] Hu Q, Wu H, Sun J, Yan D, Gao Y and Yang J 2016 *Nanoscale* **8** 5350
[122] Zhuo S, Zhang J, Shi Y, Huang Y and Zhang B 2015 *Angew. Chem. Int. Ed.* **54** 5693
[123] Deng W, Huang L, Xu X, Zhang X, Jin X, Lee S T and Jie J 2017 *Nano Lett.* **17** 2482
[124] Im J H, Lee C R, Lee J W, Park S W and Park N G 2011 *Nanoscale* **3** 4088
[125] Nozik A J 2009 *Nat. Nanotechnol.* **4** 548
[126] Lee J S, Kovalenko M V, Huang J, Chung D S and Talapin D V 2011 *Nat. Nanotechnol.* **6** 348
[127] Keuleyan S, Lhuillier E, Brajuskovic V and Guyot-Sionnest P 2011 *Nat. Photon.* **5** 489
[128] Clifford J P, Konstantatos G, Johnston K W, Hoogland S, Levina L and Sargent E H 2009 *Nat. Nanotechnol.* **4** 40
[129] Levchuk I, Osvet A, Tang X, Brandl M, Perea J D, Hoegl F, Matt G J, Hock R, Batentschuk M and Brabec C J 2017 *Nano Lett.* **17** 3993
[130] Zhang F, Zhong H, Chen C, Wu X G, Hu X, Huang H, Han J, Zou B and Dong Y 2015 *ACS Nano* **9** 4533
[131] Protesescu L, Yakunin S, Bodnarchuk M I, Krieg F, Caputo R, Hendon C H, Yang R X, Walsh A and Kovalenko M V 2015 *Nano Lett.* **15** 3692
[132] Jellicoe T C et al 2016 *J. Am. Chem. Soc.* **138** 2941
[133] Schmidt L C, Pertegás A, González-Carrero S, Malinkiewicz O, Agouram S, Mínguez Espallargas G, Bolink H J, Galian R E and Pérez-Prieto J 2014 *J. Am. Chem. Soc.* **136** 850
[134] Song J, Li J, Li X, Xu L, Dong Y and Zeng H 2015 *Adv. Mater.* **27** 7162
[135] Zhou L, Yu K, Yang F, Zheng J, Zuo Y, Li C, Cheng B and Wang Q 2017 *Dalton Trans.* **46** 1766
[136] Jang D M, Park K, Kim D H, Park J, Shojaei F, Kang H S, Ahn J P, Lee J W and Song J K 2015 *Nano Lett.* **15** 5191
[137] Dong Y, Gu Y, Zou Y, Song J, Xu L, Li J, Xue J, Li X and Zeng H 2016 *Small* **12** 5622
[138] Kwak D H, Lim D H, Ra H S, Ramasamy P and Lee J S 2016 *RSC Adv.* **6** 65252
[139] Jang D M, Kim D H, Park K, Park J, Lee J W and Song J K 2016 *J. Mater. Chem. C* **4** 10625
[140] Ramasamy P, Lim D H, Kim B, Lee S H, Lee M S and Lee J S 2016 *Chem. Commun.* **52** 2067
[141] Qin X, Yao Y, Dong H, Zhen Y, Jiang L and Hu W 2016 *Chem. Asian J.* **11** 2675
[142] Li X et al 2017 *ACS Nano* **11** 2015
[143] Song J, Xu L, Li J, Xue J, Dong Y, Li X and Zeng H 2016 *Adv. Mater.* **28** 4861
[144] Lv L et al 2016 *Nanoscale* **8** 13589
[145] Liu J et al 2016 *ACS Nano* **10** 3536
[146] Zheng W, Lin R, Zhang Z, Liao Q, Liu J and Huang F 2017 *Nanoscale* **9** 12718
[147] Saidaminov M I, Mohammed O F and Bakr O M 2017 *ACS Energy Lett.* **2** 889
[148] Cao D H, Stoumpos C C, Farha O K, Hupp J T and Kanatzidis M G 2015 *J. Am. Chem. Soc.* **137** 7843
[149] Stoumpos C C, Cao D H, Clark D J, Young J, Rondinelli J M, Jang J I, Hupp J T and Kanatzidis M G 2016 *Chem. Mater.* **28** 2852
[150] Huo C, Cai B, Yuan Z, Ma B and Zeng H 2017 *Small Methods* **1** 1600018
[151] Wang G et al 2015 *Sci. Adv.* **1** e1500613
[152] Mitzi D B 1996 *Chem. Mater.* **8** 791
[153] Dou L et al 2015 *Science* **349** 1518
[154] Zhou J, Chu Y and Huang J 2016 *ACS Appl. Mater. Interfaces* **8** 25660
[155] Koppens F H L, Mueller T, Avouris P, Ferrari A C, Vitiello M S and Polini M 2014 *Nat. Nanotechnol.* **9** 780
[156] Lee Y B, Kim S K, Lim Y R, Jeon I S, Song W, Myung S, Lee S S, Lim J and An K S 2017 *ACS Appl. Mater. Interfaces* **9** 15031
[157] He M, Chen Y, Liu H, Wang J, Fang X and Liang Z 2015 *Chem. Commun.* **51** 9659
[158] Wang Y et al 2015 *Adv. Opt. Mater.* **3** 1389
[159] Ma C, Shi Y, Hu W, Chiu M H, Liu Z, Bera A, Li F, Wang H, Li L J and Wu T 2016 *Adv. Mater.* **28** 3683
[160] Song X et al 2018 *ACS Appl. Mater. Interfaces* **10** 2801
[161] Liu F, Wang J, Wang L, Cai X, Jiang C and Wang G 2017 *J. Semicond.* **38** 034002
[162] Shao Y et al 2017 *Nano Lett.* **17** 7330
[163] Qian L, Sun Y, Wu M, Xie D, Ding L and Shi G 2017 *Adv. Mater.* **29** 1606175
[164] Niu L et al 2015 *Adv. Mater.* **27** 7800
[165] Qian L, Sun Y, Wu M, Li C, Xie D, Ding L and Shi G 2018 *Nanoscale* **10** 6837
[166] Tan Z et al 2016 *J. Am. Chem. Soc.* **138** 16612
[167] Xia H, Tong S, Zhang C, Wang C, Sun J, He J, Zhang J, Gao Y and Yang J 2018 *Appl. Phys. Lett.* **112** 233301
[168] Liu C, Wang K, Yi C, Shi X, Du P, Smith A W, Karim A and Gong X 2015 *J. Mater. Chem. C* **3** 6600
[169] Shen Y, Yu D, Wang X, Huo C, Wu Y, Zhu Z and Zeng H 2018 *Nanotechnology* **29** 085201
[170] Luan S Z, Wang Y C, Liu Y T and Jia R X 2018 *Chin. Phys. B* **27** 047208
[171] Chen S, Teng C, Zhang M, Li Y, Xie D and Shi G 2016 *Adv. Mater.* **28** 5969
[172] Teng C J, Xie D, Sun M X, Chen S, Yang P and Sun Y L 2016 *ACS Appl. Mater. Interfaces* **8** 31289
[173] Anaraki E H et al 2016 *Energy Environ. Sci.* **9** 3128
[174] Domanski K, Tress W, Moehl T, Saliba M, Nazeeruddin M K and Grätzel M 2015 *Adv. Funct. Mater.* **25** 6936
[175] Yu J et al 2016 *J. Mater. Chem. C* **4** 7302
[176] Xue M, Zhou H, Xu Y, Mei J, Yang L, Ye C, Zhang J and Wang H 2017 *Sci. Chin. Mater.* **60** 407
[177] Alwadai N, Haque M A, Mitra S, Flemban T, Pak Y, Wu T and Roqan I 2017 *ACS Appl. Mater. Interfaces* **9** 37832
[178] Dong J, Xu X, Shi J J, Li D M, Luo Y H, Meng Q B and Chen Q 2015 *Chin. Phys. Lett.* **32** 078401

[179] Zhu H L, Cheng J, Zhang D, Liang C, Reckmeier C J, Huang H, Rogach A L and Choy W C H 2016 *ACS Nano* **10** 6808
[180] Rim Y S, Yang Y, Bae S H, Chen H, Li C, Goorsky M S and Yang Y 2015 *Adv. Mater.* **27** 6885
[181] Du S, Li G, Cao X, Wang Y, Lu H, Zhang S, Liu C and Zhou H 2017 *Adv. Electron. Mater.* **3** 1600325
[182] Gao J, Nguyen S C, Bronstein N D and Alivisatos A P 2016 *ACS Photon.* **3** 1217
[183] Sukhovatkin V, Hinds S, Brzozowski L and Sargent E H 2009 *Science* **324** 1542
[184] Hsiao Y J, Ji L W, Lu H Y, Fang T H and Hsiao K H 2017 *IEEE Sens. J.* **17** 3710
[185] Liu C, Peng H, Wang K, Wei C, Wang Z and Gong X 2016 *Nano Energy* **30** 27
[186] Sulaman M, Yang S, Jiang Y, Tang Y and Zou B 2017 *Nanotechnology* **28** 505501
[187] Peng B et al 2016 *ACS Nano* **10** 6383
[188] Rim Y S, Bae S H, Chen H, De Marco N and Yang Y 2016 *Adv. Mater.* **28** 4415
[189] Han S T, Peng H, Sun Q, Venkatesh S, Chung K S, Lau S C, Zhou Y and Roy V A L 2017 *Adv. Mater.* **29** 1700375
[190] Xie C and Yan F 2017 *Small* **13** 1701822
[191] Wu X, Zhou B, Zhou J, Chen Y, Chu Y and Huang J 2018 *Small* **14** 1800527
[192] Okubo T, Nakagawa N and Tsuchida A 2007 *Colloid Polym. Sci.* **285** 1247
[193] Dandin M, Abshire P and Smela E 2007 *Lab Chip* **7** 955
[194] Han M G et al 2016 *ACS Appl. Mater. Interfaces* **8** 26143
[195] Sobhani A, Knight M W, Wang Y, Zheng B, King N S, Brown L V, Fang Z, Nordlander P and Halas N J 2013 *Nat. Commun.* **4** 1643
[196] Nishiwaki S, Nakamura T, Hiramoto M, Fujii T and Suzuki M A 2013 *Nat. Photon.* **7** 240
[197] Armin A, Jansen-Van Vuuren R D, Kopidakis N, Burn P L and Meredith P 2015 *Nat. Commun.* **6** 6343
[198] Rao H S, Li W G, Chen B X, Bin D and Su C Y 2017 *Adv. Mater.* **29** 1602639
[199] Li L, Deng Y, Bao C, Fang Y, Wei H, Tang S, Zhang F and Huang J 2017 *Adv. Opt. Mater.* **5** 1700672
[200] Qiao K, Deng H, Yang X, Dong D, Li M, Hu L, Liu H, Song H and Tang J 2016 *Nanoscale* **8** 7137
[201] Feng J et al 2018 *Nat. Electron.* **1** 404
[202] Tong G, Li H, Li D, Zhu Z, Xu E, Li G, Yu L, Xu J and Jiang Y 2018 *Small* **14** 1702523
[203] Chen Q, Zhou H, Bin T, Luo S, Hong Z, Duan H S, Dou L, Liu Y and Yang Y 2014 *Nano Lett.* **14** 4158
[204] Zheng Z, Zhuge F, Wang Y, Zhang J, Gan L, Zhou X, Li H and Zhai T 2017 *Adv. Funct. Mater.* **27** 1703115
[205] Yang Z, Wang M, Li J, Dou J, Qiu H and Shao J 2018 *ACS Appl. Mater. Interfaces* **10** 26387
[206] Cheng H C, Wang G, Li D, He Q, Yin A, Liu Y, Wu H, Ding M, Huang Y and Duan X 2016 *Nano Lett.* **16** 367
[207] Peng W, Yu R, Wang X, Wang Z, Zou H, He Y and Wang Z L 2016 *Nano Res.* **9** 3695
[208] Su L, Zhao Z X, Li H Y, Yuan J, Wang Z L, Cao G Z and Zhu G 2015 *ACS Nano* **9** 11310
[209] Bao C, Zhu W, Yang J, Li F, Gu S, Wang Y, Yu T, Zhu J, Zhou Y and Zou Z 2016 *ACS Appl. Mater. Interfaces* **8** 23868
[210] Leung S F, Ho K T, Kung P K, Hsiao V K S, Alshareef H N, Wang Z L and He J H 2018 *Adv. Mater.* **30** 1704611
[211] Zhang J, Yu C, Wang L, Li Y, Ren Y and Shum K 2015 *Sci. Rep.* **4** 6954
[212] Stoumpos C C, Malliakas C D and Kanatzidis M G 2013 *Inorg. Chem.* **52** 9019
[213] Ogomi Y et al 2014 *J. Phys. Chem. Lett.* **5** 1004
[214] Milot R L, Eperon G E, Green T, Snaith H J, Johnston M B and Herz L M 2016 *J. Phys. Chem. Lett.* **7** 4178
[215] Li J, Shen Y, Liu Y, Shi F, Ren X, Niu T, Zhao K and Liu S F 2017 *ACS Appl. Mater. Interfaces* **9** 19176
[216] Jang Y J, Kim E, Ahn S, Chung K, Kim J, Kim H, Wang H, Lee J, Kim D W and Kim D H 2017 *J. Phys. Chem. Lett.* **8** 364
[217] Zhang Z X, Tong X W, Gao Y, Xie C, Tsang Y H, Luo L B and Wu Y C 2018 *J. Phys. Chem. Lett.* **9** 1185
[218] Wang Z, Lin Q, Chmiel F P, Sakai N, Herz L M and Snaith H J 2017 *Nat. Energy* **2** 17135
[219] Lin Y, Bai Y, Fang Y, Chen Z, Yang S, Zheng X, Tang S, Liu Y, Zhao J and Huang J 2018 *J. Phys. Chem. Lett.* **9** 654
[220] Grancini G et al 2017 *Nat. Commun.* **8** 15684
[221] Zhu P, Gu S, Shen X, Xu N, Tan Y, Zhuang S, Deng Y, Lu Z, Wang Z and Zhu J 2016 *Nano Lett.* **16** 871
[222] Lin Y, Lin G, Sun B and Guo X 2018 *Adv. Funct. Mater.* **28** 1705589